Elucidation of the Structural and Optical Properties of Metal Cation (Na^+, K^+, and Bi^{3+}) Incorporated $Cs_2AgInCl_6$ Double Perovskite Nanocrystals†‡

Parth Vashishtha*[†⁋⊥], Benjamin E. Griffith[‖†⊥], Yanan Fang[†], Ankit Jaiswal[†], Gautam V. Nutan[†], Albert P. Bartók[‖§], Tim White[†] and John V. Hanna*[‖†]

[⊥]**P.V. and B.E.G. contributed equally to this work**

[†] School of Materials Science and Engineering, Nanyang Technological University, 50 Nanyang Avenue, Singapore 639798, Republic of Singapore

[⁋] Quantum Science Ltd, Techspace One, Daresbury, Warrington, WA4 4AB, United Kingdom

[‖] Department of Physics, University of Warwick, Coventry CV4 7AL, United Kingdom

[§] Warwick Centre for Predictive Modelling, School of Engineering, University of Warwick, Coventry CV4 7AL, United Kingdom

Corresponding Authors: PVashishtha@ntu.edu.sg
J.V.Hanna@warwick.ac.uk

† The experimental data for this study are provided as a supporting dataset from WRAP, the Warwick Research Archive Portal at http://wrap.warwick.ac.uk/160748/.

‡ Electronic supplementary information (ESI) available: Supporting experimental and materials characterization including fully detailed synthesis and instrumental/measurement descriptions, TEM images with particle size and EDXS elemental analyses, measured ^{133}Cs and ^{39}K MAS NMR spectra with tabulated shift, intensity and T_1 data, diagrammatic representation of the T_1 regimes encountered for each system, powder XRD data, and calibration curves relating the ^{133}Cs and ^{39}K experimentally measured shifts and the DFT calculated shieldings. See DOI:10.1039/XXXXXXXX.

Abstract

This study presents series of direct band gap Pb-free double perovskite $Cs_2AgIn_xBi_{1-x}Cl_6$, $Cs_2Na_xAg_{1-x}InCl_6$:Bi and $Cs_2K_xAg_{1-x}InCl_6$:Bi nanocrystal systems [Cs_2B'(I)B''(III)Cl_6] synthesised using a colloidal hot-injection route. The structural properties investigated using powder XRD, TEM, solid state NMR and materials modelling approaches demonstrate that the incorporation of K^+ cations into double perovskite nanocrystal structure occurs simultaneously on both the Cs (A) site and Ag (B'(I)) positions within a series of closely related cubic and monoclinic structures. As a result of defect passivation, significant improvements in the photoluminescence quantum yield (PLQY) of ~4.7× and ~1.8× are exhibited in comparison to the $Cs_2AgIn_xBi_{1-x}Cl_6$, and $Cs_2Na_xAg_{1-x}InCl_6$:Bi nanocrystal systems, respectively. Materials modelling using the *Ab Initio* Random Structure Search (AIRSS) method, and the GIPAW DFT calculation of the NMR parameters from the derived structural realisations, shows that K^+ incorporation induces significant short-range structural disorder and multi-phase formation. This is highlighted by the large ^{133}Cs and ^{39}K chemical shift dispersion characterising the MAS NMR data. Density of States (DoS) calculations describing these AIRSS generated structures suggest that increasing ionic character and reduced structural rigidity is strongly correlated with A site substitution of the K^+ cation into these cubic and monoclinic phases. The ^{39}K MAS NMR data reveals that the increasing PLQY performance maps directly with the K^+ incorporation into the cubic $CsK_yAg_{1-y}InCl_6$ phase supporting B site occupancy which is observed to be maximized at a 60 ml% K^+ incorporation level. However, additional evidence indicates that low level K^+ substitution primarily targets A site occupancy in a surface passivation role. The improvement to the optical properties induced by K^+ and Na^+ incorporation is rationalised in terms of increased covalent character and structural rigidity associated with decreased Cs^+, Na^+

and K^+ cation mobility, as evidenced by the large (~2 orders of magnitude) variation in the ^{133}Cs T_1 data across each compositional range.

Introduction

Metal halide perovskite (ABX_3) nanocrystals offer several advantages over bulk materials due to their thin emission linewidths, stable crystal structure due to the presence of passivation ligands, high photoluminescence quantum yield, high absorption cross-section, and surface functionality as a result of quantum confinement.[1-5] The most efficient perovskite nanocrystals such as, $CsPbX_3$ (X= Br, Cl, I), $FAPbX_3$, $MAPbX_3$, $Cs_{0.05}(FA_{0.83}MA_{0.17})_{0.95}PbX_3$ and $Zn^{2+}/CsPbBr_3$ demonstrate emission throughout the visible spectrum (400 - 760 nm) and high photoluminescence quantum yield, making these materials of high interest for optoelectronic applications.[5-10] Light emitting diodes and solar cells based on these metal halide perovskites have shown excellent performance with efficiencies of nearly 25% power conversion efficiency (PCE) of solar cells and 20% external quantum efficiency (EQE) of LEDs.[4, 11-19] However, these families of perovskites contain Pb which limits the commercial viability of these materials due to its environmental incompatibility and toxicity.[17] The subsequent development of Pb-free perovskite systems has been extensive; however, the performance of these materials is inferior to their Pb-containing analogues.[20, 21] For example, Sn-based alternatives such as $CsSnX_3$ (X = Cl, Br, I) offer one alternative, although the instability of the Sn^{2+} oxidation state, and its propensity to transform to the Sn^{4+} state under ambient conditions, destabilizes these systems.[20] In addition, $CsSnX_3$ nanocrystal systems do not exhibit the necessary quantum yields or local structural stability due to the presence of intrinsic crystal defects.[22] The further development of Pb-free alternatives has explored the incorporation of other metal cations such as Sb, Bi and Cu, but these have not been fully examined to ascertain their suitability in optoelectronic applications.[23-27]

In contrast, Pb-free pure inorganic double perovskite structures such as indirect band gap $Cs_2AgBiCl_6$ and direct band gap $Cs_2AgInCl_6$ systems were recently investigated and found to have high structural stability under ambient conditions.[24, 28-30] While $Cs_2AgBiCl_6$ nanocrystal systems deliver low photoluminescence quantum yield due to the indirect band gap caused by its intrinsic properties,[31, 32] the direct band gap analogue $Cs_2AgInCl_6$ is a more suitable candidate for optoelectronic applications. This latter system has received widespread attention since the first report of its bulk structure.[28-30, 33] Locardi *et al.* were the first to report quantum confined $Cs_2AgInCl_6$ colloidal nanocrystals synthesised using a hot-injection route; these assumed a cubic $Fm\bar{3}m$ crystal structure and demonstrated an experimental direct optical band gap of 4.7 eV.[30] However, the photoluminescence quantum yield of $Cs_2AgInCl_6$ was found to be extremely low (1.6%) due to parity-forbidden transitions from the direct valence band maximum (VBM) to conduction band minimum (CBM) at the Γ point, as per the Laporte rule.[34, 35] Moreover, the large difference between experimental band gap (4.7 eV) and calculated band gap (2.7 eV) is also attributed to the fact that the direct band gap transitions are parity forbidden. [30] However, bismuth doped $Cs_2AgInCl_6$ has been found to have less surface defects resulting in enhanced radiative localisation and thus increased photoluminescence quantum yield (~ 11%) in the broad band orange spectral region.[28, 29] The cause of broad band emission can be attributed to the Jahn-Teller distortion of the $[AgCl_6]^{5-}$ octahedron in excited molecular states, or due to the presence of self-trapped excitons.[28, 36] Nevertheless, the incorporation of Bi^{3+} in direct band gap $Cs_2AgInCl_6$ has led to improved optical properties. This has motivated many studies towards the substitution of the $Cs_2AgInCl_6$ framework with metal cations such as Na^+, Ga^+, Cr^{3+}, Ce^{3+} and Sb^{2+} to find improved photoluminescence properties.[37-43] Na^+ doping in $Cs_2AgInCl_6$:Bi has significantly improved the photoluminescence quantum yield in bulk thin-films as well as nanocrystals up to 85% and 22%, respectively.[39, 40] However, there is still a need to precisely tune both the structural and optical properties of these systems formed through systematic doping of the metal cation. A recent study by Karmakar *et al.* has shown the importance of investigating the localised structural environments in $Cs_2Bi_{1-x}In_xAgCl_6$:Sb bulk materials and their relations to PL improvements.[44] Investigations using the solid state NMR technique have demonstrated that direct observation of the atomic ordering phenomena of the B''(III)/B'(I) octahedra is possible, thus allowing insights into how dopants are being incorporated into the double perovskite structure. More importantly, the local structure of Na^+ and K^+ doped $Cs_2AgInCl_6$ doped double perovskite nanocrystals have never been explored using solid state NMR; these are crucial developments that could underpin the improvement in the functionality of these materials.

In this work, series of $Cs_2AgInCl_6$ nanocrystals have been synthesized with varying amounts of Bi^{3+}, Na^+ and K^+ cations incorporated using a colloidal hot-injection route. Initially, the structural and optical properties of $Cs_2AgIn_xBi_{1-x}Cl_6$ (x = 0.1 - 1) nanocrystal system have been investigated as a baseline material. Subsequent studies involved the synthesis and systematic characterisation of the $Cs_2Ag_xNa_{1-x}InCl_6$:Bi (x = 0 - 1) and $Cs_2Ag_xK_{1-x}InCl_6$:Bi (x = 0 - 1) series, where the powder XRD and multinuclear solid state NMR techniques were employed to interrogate the long range periodicity and short range localised structures comprising these materials, respectively. For the case of K^+ incorporation, materials modelling using the *Ab Initio* Random Structure Search (AIRSS) method,[45] and the calculation of the NMR parameters emanating from the generated structural realisations using the GIPAW DFT approach have been introduced to elucidate further insights from the interpretation of both the solid state NMR and powder XRD data.[46-48] The effect of Na^+ and K^+ doping on the optical and structural properties of $Cs_2AgInCl_6$:Bi baseline nanocrystal systems has been investigated.

Results & Discussion

$Cs_2AgIn_xBi_{1-x}Cl_6$ (x = 0 - 1) Nanocrystal System

Nanocrystals were synthesised using a colloidal hot-injection route in which an appropriate quantity of acetate metal salts were dissolved in a reaction flask containing di-phenyl ether with suitable ligands followed by the hot-injection of benzoyl chloride into the reaction flask at 115 °C under inert atmosphere (see the Experimental section in the SI for details). Firstly, double perovskite nanocrystals with $Cs_2AgIn_xBi_{1-x}Cl_6$ (x = 0 - 1) composition were prepared as baseline materials to optimize the amount of bismuth. Powder X-ray diffraction data of Figure 1a confirms the formation of a cubic $Cs_2AgInCl_6$ perovskite phase. As expected, Bi incorporation into the $Cs_2AgInCl_6$ structure expands the structural parameters, thus inducing a monotonic shift in the observed reflections towards lower angle (see Figures 1b and 1c). As shown in Figures 1d and S1a, the TEM micrographs of the $Cs_2AgIn_{0.90}Bi_{0.10}Cl_6$ and $Cs_2AgIn_{0.50}Bi_{0.50}Cl_6$ nanocrystals depict the cubic morphology of these nanocrystals with average particle diameters of ~17 nm and 15 nm, respectively. High resolution TEM micrographs of Figure 1d exhibit resolved lattice fringes and the fast Fourier transform (FFT) of cubic the nanocrystals corresponding to the (022) crystal plane of the perovskite framework. Overall, the matching of FFT and lattice spacing d with the (022) plane of XRD pattern validates the structure of these nanocrystal systems. Figures 1e and 1f illustrate the absorption and PL characteristics from the $Cs_2AgIn_xBi_{1-x}Cl_6$ (x = 0 - 1) suite of nanocrystals, with the observed excitonic peak at 367 - 368 nm observed in all spectra resulting from direct s-p transitions as reported in previous studies on these nanocrystal systems.[28, 49] However, pure $Cs_2AgInCl_6$ nanocrystals exhibit a weak absorption at 360 nm together with a strong absorption feature below 300 nm attributed to the parity-forbidden direct transition in this material; this is an intrinsic property of the $Cs_2AgInCl_6$ system.[23] In contrast, as demonstrated from Figure 1f pure $Cs_2AgInCl_6$ nanocrystals do not exhibit photoluminescence behaviour as this system is an indirect band gap semiconductor. This observation is consistent with previous literature reports.[28, 50] As evident from the range of PL data exhibited in Figure 1f, pure $Cs_2AgInCl_6$ shows a blue emission near 400 nm, however the introduction of Bi^{3+} at dopant levels as low as 0.5 mol% induces an orange emission at 581 nm which becomes red-shifted to 590 nm with increasing Bi^{3+} content. The images presented in Figure 1g show the stimulated emission from the 100 % and 90 % In containing samples under 365 nm UV illumination, illustrating the change in emission colour with addition of dopant levels of Bi^{3+} in the perovskite structure. The photoluminescence quantum yield (PLQY) of each nanocrystal sample was measured and it was found that the 90 % In/10 %Bi containing sample exhibited the highest PLQY of 8 %, whereas the 99.5 % In/0.5 % Bi doped sample showed the second highest PLQY of 6 %.

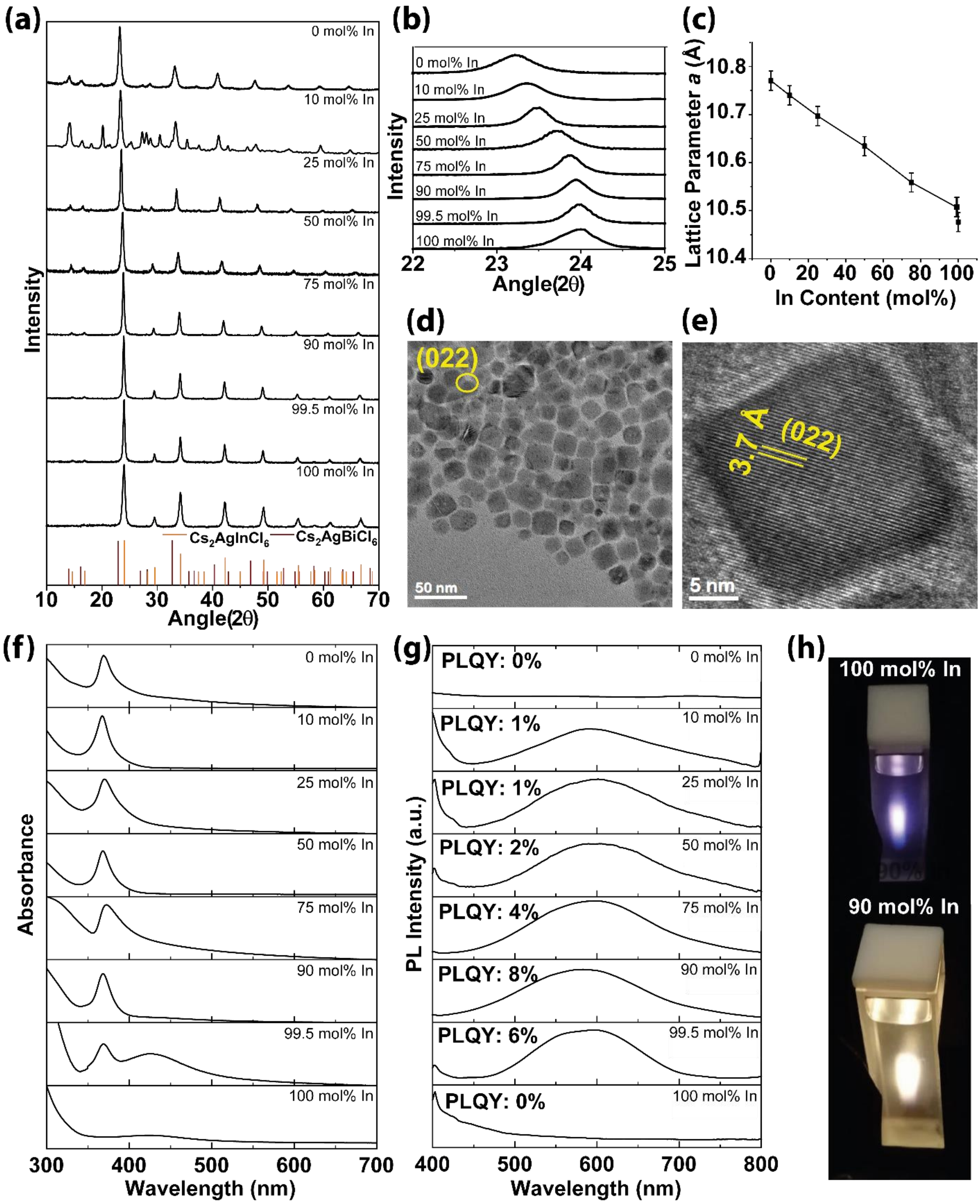

Figure 1. Characterisation data of the $Cs_2AgIn_xBi_{1-x}Cl_6$ (x = 0 - 1) nanocrystal series including, (a) powder XRD data (b) an expansion of (022) reflection showing the peak shift as a function of In composition, (c) the change in lattice parameter *a* with In content extracted from XRD refinement, (d) a low resolution TEM micrograph of $Cs_2AgIn_{0.90}Bi_{0.10}Cl_6$ nanocrystals, (e) a high resolution TEM of the same sample depicting the lattice fringes and fast Fourier transform (FFT), (f) absorption and (g) photoluminescence (PL) spectra of $Cs_2AgIn_xBi_{1-x}Cl_6$ nanocrystals solution dispersed in hexane with PL quantum labelled in each spectrum, and (h) photographs of 100 and 90 mol% In^{3+} preparations under 365 nm UV excitation.

While it has been demonstrated that the incorporation of Bi^{3+} (even at dopant levels of 0.5 mol% Bi^{3+}) improves the PLQY of these nanocrystals, it is important to observe from Figures 1a and 1b that this dopant level substitution does not perturb the overall crystal structure and lattice parameters characterising the $Cs_2AgInCl_6$ nanocrystal system. Nevertheless, it still induces significant improvement in the PL properties including orange emission. Based on these characteristics Bi^{3+} doped preparations have been adopted for further compositional engineering in these nanocrystal systems, with previous reports proposing that the improvement in optical properties via Bi^{3+} incorporation could be due to improved short range crystalline order and excitonic localisation.[28, 51]

The ^{133}Cs solid state MAS NMR technique was implemented to examine the short range structural effects introduced by Bi^{3+} incorporation in the $Cs_2AgIn_xBi_{1-x}Cl_6$ (x = 0 - 1) compositional range. The data characterising these systems presented in the Figures 2a-c, Figure S2, and Table S1 exhibit similarities to those reported by Karmakar *et al.* who investigated the bulk materials structures; these assignments were adopted in order to assign the Cs speciation observed in the nanocrystalline materials.[44] Each structure within the $Cs_2In_xBi_{1-x}AgCl_6$ compositional series can be described as Cs positions located in cubooctahedral environments surrounded by four $[AgCl_6]^{5-}$ octahedra, alternating with four $[InCl_6]^{3-}$ or $[BiCl_6]^{3-}$ octahedra. The narrow ^{133}Cs resonances characterising these data reflect the high point symmetry defining the Cs^+ nearest-neighbour environments. From Figure 2a the single resonances observed at δ 128 ppm and δ 82 ppm from the pure $Cs_2InAgCl_6$ and $Cs_2BiAgCl_6$ end members are ascribed to Cs^+ cations surrounded by four $[InCl_6]^{3-}$ or four $[BiCl_6]^{3-}$ neighbouring octahedra, respectively. The ^{133}Cs chemical shifts associated with the evolving Cs speciation within the intermediate $Cs_2In_xBi_{1-x}AgCl_6$ (x = 0.10 - 0.95) compositional series reflect the diverse combinations of Cs surrounded by $[InCl_6]^{3-}$ and $[BiCl_6]^{3-}$ octahedra. At the 50 mol% Bi^{3+} substitution level, five discrete Cs positions are observed. While the resonances at δ 87 ppm and δ 188 ppm are the shifted variants of the $Cs_2BiAgCl_6$ and $Cs_2InAgCl_6$ end member species, the three remaining ^{133}Cs resonances at δ 109, 102 and 96 ppm are assigned to the four $[InCl_6]^{3-}$ octahedra substituted by one, two and three $[BiCl_6]^{3-}$ octahedra in neighbouring positions, respectively. The measured ^{133}Cs chemical shifts are directly influenced by the varying quantities of the Bi^{3+} substituent on the In^{3+} position; as the Bi^{3+} content increases the ^{133}Cs isotropic chemical shift becomes increasingly deshielded and moves linearly to higher frequencies/lower ppm due to the decreasing electron density at the Cs^+ positions governed by the concomitant lattice expansion. This behaviour corroborates the PXRD study shown in Figure 1b. Note that the ^{133}Cs resonance linewidths exhibited in Figures 2a and S2 broaden significantly at intermediate Bi^{3+} doping levels due to the increased local structural disorder induced by the dispersion of next-nearest-neighbour environments.

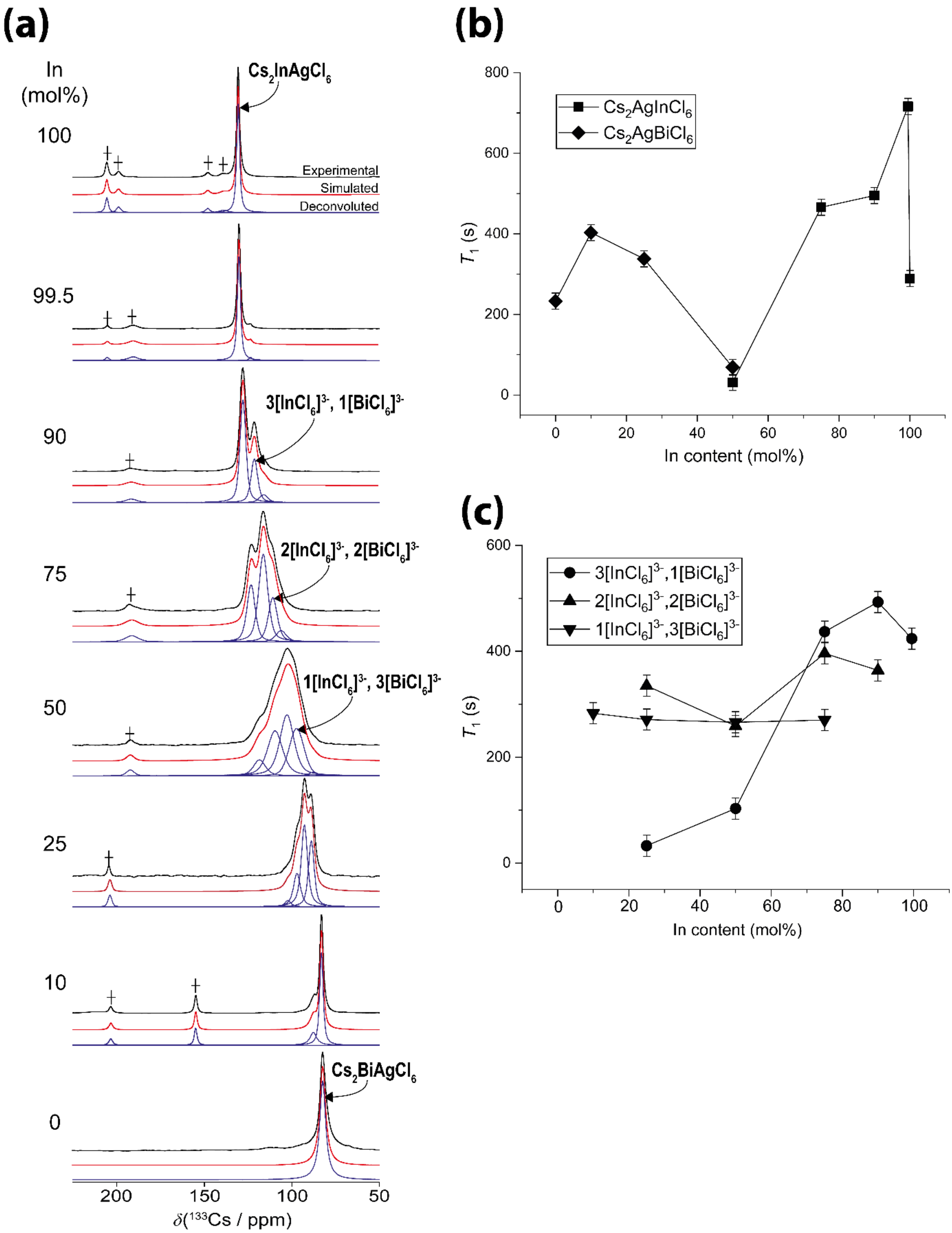

Figure 2. ^{133}Cs MAS NMR data (B_0 = 14.1 T, ν_r = 12 kHz) from the $Cs_2In_xBi_{1-x}AgCl_6$ (x = 0 - 1) nanocrystal series showing, (a) the deconvolution, spectral simulations and resonance assignments indicating the different octahedral arrangements comprising each Cs environment (impurities are indicated by '†'), (b) and (c) the trends in the T_1 relaxation times trends for each Cs environment. The ^{133}Cs T_1 relaxation times are determined by the saturation-recovery technique.

The mobility of each Cs environment was investigated through the measurement of ^{133}Cs of spin-lattice (T_1) relaxation times, exhibited in Figures 2b and 2c as a function of In^{3+} content in Figures 2b and 2c. The very small electric quadrupole moment characterising the I = 7/2 ^{133}Cs nucleus, the absence of chemical shift variation with change of external B_0 field, and the increase of the ^{133}Cs linewidth with B_0 (see Figures S2 and Table S1) collectively indicate that the ^{133}Cs MAS NMR linewidths are dominated by chemical shift dispersion. Furthermore, the $1/B_0$ dependence of the measured T_1 values (see Table S1) suggests that these values are governed by a dipolar relaxation mechanism that is schematically represented in Figure S3, thus reflecting the dynamics and mobility characterising each Cs^+ cation position.

From Figure 2b it is important to observe that the Bi^{3+}-rich compositions represented by the $Cs_2BiAgCl_6$ resonance (δ 83 - 88 ppm in Figure 2a, denoted with a ♦ in Figure 2b) and the In^{3+}-rich compositions represented by the $Cs_2InAgCl_6$ resonance (δ 118 - 128 ppm in Figure 2a, denoted with a ■ in Figure 2b) exhibit ^{133}Cs T_1 values that are 2 - 3 orders of magnitude greater than the those representing the mid-range ~50 mol% In^{3+} compositions. This result demonstrates that greater Cs^+ mobility is facilitated by increased structural disorder generated in this region of the compositional range. The decrease in the measured ^{133}Cs T_1 values as the $Cs_2BiAgCl_6$ and $Cs_2InAgCl_6$ end-member compositions are approached suggests that small quantities of In^{3+} within the $Cs_2BiAgCl_6$ system, and Bi^{3+} within the $Cs_2InAgCl_6$ system, induce distinct passivation effects within these structures. Dopant-level incorporation of ~0.5 mol% Bi^{3+} stimulates an increase in T_1 from ~290 to 720 s, thus highlighting the efficiency of this species in passivating structural defects and vacancies and restricting Cs^+ mobility. This effect is correlated with the strong orange emission at ~580 nm dominating the PL properties up to a composition of 99.5 mol% In^{3+} which subsequently disappears at 100 mol% In^{3+}.

The ^{133}Cs MAS NMR data spanning the intermediate compositional range (i.e. ~25 - 75 mol% In^{3+}) suggests that the Cs speciation is dominated by structural disorder defined by the relative nearest-neighbour octahedral substitution surrounding each Cs^+ cation position. These environments are defined as $1[InCl_6]^{3-}$,$3[BiCl_6]^{3-}$, $2[InCl_6]^{3-}$,$2[BiCl_6]^{3-}$ and $3[InCl_6]^{3-}$,$1[BiCl_6]^{3-}$ positions. Figure 2c indicates that the Cs^+ mobility and response to compositional change is inhomogeneous and complex; these data show the ^{133}Cs T_1 of the Bi^{3+}-rich $1[InCl_6]^{3-}$,$3[BiCl_6]^{3-}$ environment to be invariant to composition, the Bi^{3+}/In^{3+}-neutral $2[InCl_6]^{3-}$,$2[BiCl_6]^{3-}$ environment varies marginally with composition, while the In^{3+}-rich $3[InCl_6]^{3-}$,$1[BiCl_6]^{3-}$ exhibits a marked T_1 variation of ~460 s over the 25 - 90 mol% In^{3+} range. Like the passivation phenomenon demonstrated in the 99.5 mol% In^{3+} preparation (see above), this behaviour suggests that Cs^+ cation mobility is actively reduced (i.e. T_1s increase) with optimised passivation when Bi^{3+} concentrations are substantially reduced.

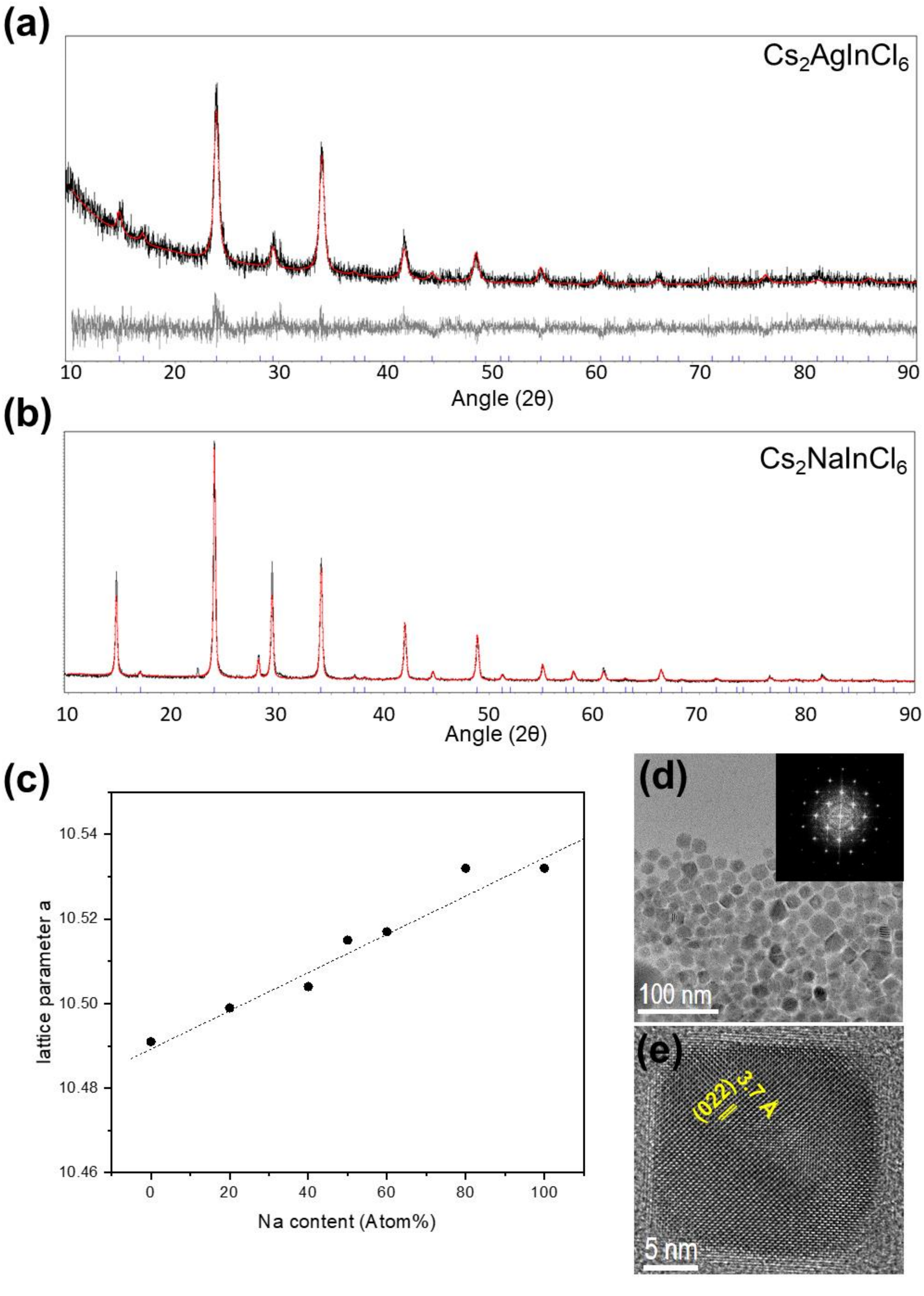

Figure 3. X-ray diffraction pattern of (a) $Cs_2AgInCl_6$:Bi and (b) $Cs_2NaInCl_6$:Bi nanocrystals, (c) Change in lattice parameters *a* with Na atomic percent extracted from XRD refinement, (d) TEM micrographs of $Cs_2Ag_{0.60}Na_{0.40}InCl_6$:Bi nanocrystals with FFT and (e) high-resolution TEM image depicting the lattice fringes of corresponding cubic nanocrystal.

$Cs_2Na_xAg_{1-x}InCl_6$:Bi (x = 0 - 1) Nanocrystal System

While the inclusion of dopant levels (~0.5 mol%) Bi^{3+} into the nominal stoichiometry optimises the photophysical performance of the nanocrystal system without inducing major structural alteration, this strategy is adopted when further exploring substituted double perovskite nanomaterials. The Na^+ cation has been reported to improve the PLQY in bulk preparations of other double perovskite systems,[39] hence a logical progression to this investigation involves the synthesis of $Cs_2AgInCl_6$ nanocrystals with different mole percentages of Na^+ incorporation onto the Ag^+ site. Figures 3a and 3b show the X-ray powder diffraction patterns of $Cs_2AgInCl_6$:Bi and $Cs_2NaInCl_6$:Bi nanocrystals which both crystallise into the cubic $Fm\bar{3}m$ space group, while Figures 3c and S4 demonstrate a linear trend in the expansion of the lattice parameter *a* with respect to increasing Na^+ content. The TEM micrographs of these nanocrystals shown in Figures 3d and 3e, and Figure S1b indicates a cubic morphology with an average particle diameter of ~14 nm as calculated by a histogram analysis. A high resolution TEM image of Figure 3e shows a lattice spacing of 3.7 Å corresponding to the (022) plane of the cubic double perovskite structure. These data closely match the TEM and XRD data of the baseline $Cs_2AgIn_xBi_{1-x}Cl_6$ nanocrystalline material as presented in Figures 1a-d.

Figures 4a and 4b show the ^{23}Na and ^{133}Cs solid state MAS NMR data, respectively, measured from the $Cs_2Na_xAg_{1-x}InCl_6$:Bi for (x = 0.2 - 1) series of nanocrystals. A single narrow resonance comprises each ^{23}Na MAS NMR spectrum which is consistent with the high symmetry octahedral $[NaCl_6]^{5-}$ environments in the cubic structure, as highlighted in XRD study above. This resonance progressively becomes more shielded, shifting from δ ~2.0 to δ ~2.5 ppm with increasing Na^+ incorporation. Similarly, a single narrow resonance is observed in each corresponding ^{133}Cs MAS NMR spectrum verifying the high symmetry octahedral $[CsCl_6]^{5-}$ environments; however, this resonance shifts from δ ~128 to δ ~121 ppm thus becoming more deshielded with increasing Na^+ substitution. These opposing trends correlate with the emerging disorder in the nearest-neighbour octahedra upon increasing Na^+ substitution which subsequently induces lattice expansion and a marked increase in the *a* lattice parameter (see Figure 3c).

From the ^{23}Na and ^{133}Cs T_1 relaxation time behaviour presented in Figures 4c and 4d, respectively, there exists ~2 - 3 orders of magnitude difference between the magnitudes of the T_1 relaxation times measured for the ^{23}Na and ^{133}Cs nuclei. These data indicate a far greater comparative mobility of Na^+ cations within this structure which is consistent with its much smaller ionic radius (~1.02 Å for Na^+ vs. ~1.67 Å for Cs^+) and propensity to avoid chemical/covalent interactions. Despite the ^{23}Na nucleus possessing a much larger quadrupole moment than its ^{133}Cs counterpart, the high cubic point symmetry ensures that the average ^{23}Na quadrupole parameters are negligible, as evidenced by the invariant chemical shifts (δ_{iso}) with change in B_0 (see Table S2). Hence, it can be inferred that a dipolar T_1 relaxation mechanism is also dominant for this nucleus. Within experimental error the ^{23}Na T_1 relaxation times appear largely invariant over the entire compositional range. In contrast, the ^{133}Cs T_1 relaxation times appear largely invariant over the 20 - 60 mol% Na range, however the >60 mol% Na range exhibits a significant decrease in T_1s of ~300 s. As evidenced by the TEM EDXS data of Table S3, a reduction in the Cs elemental ratio appears at 80 mol% Na indicating an increased Cs vacancy formation that is characterised by more rapid Cs^+ cation mobility and reduced T_1 relaxation times.

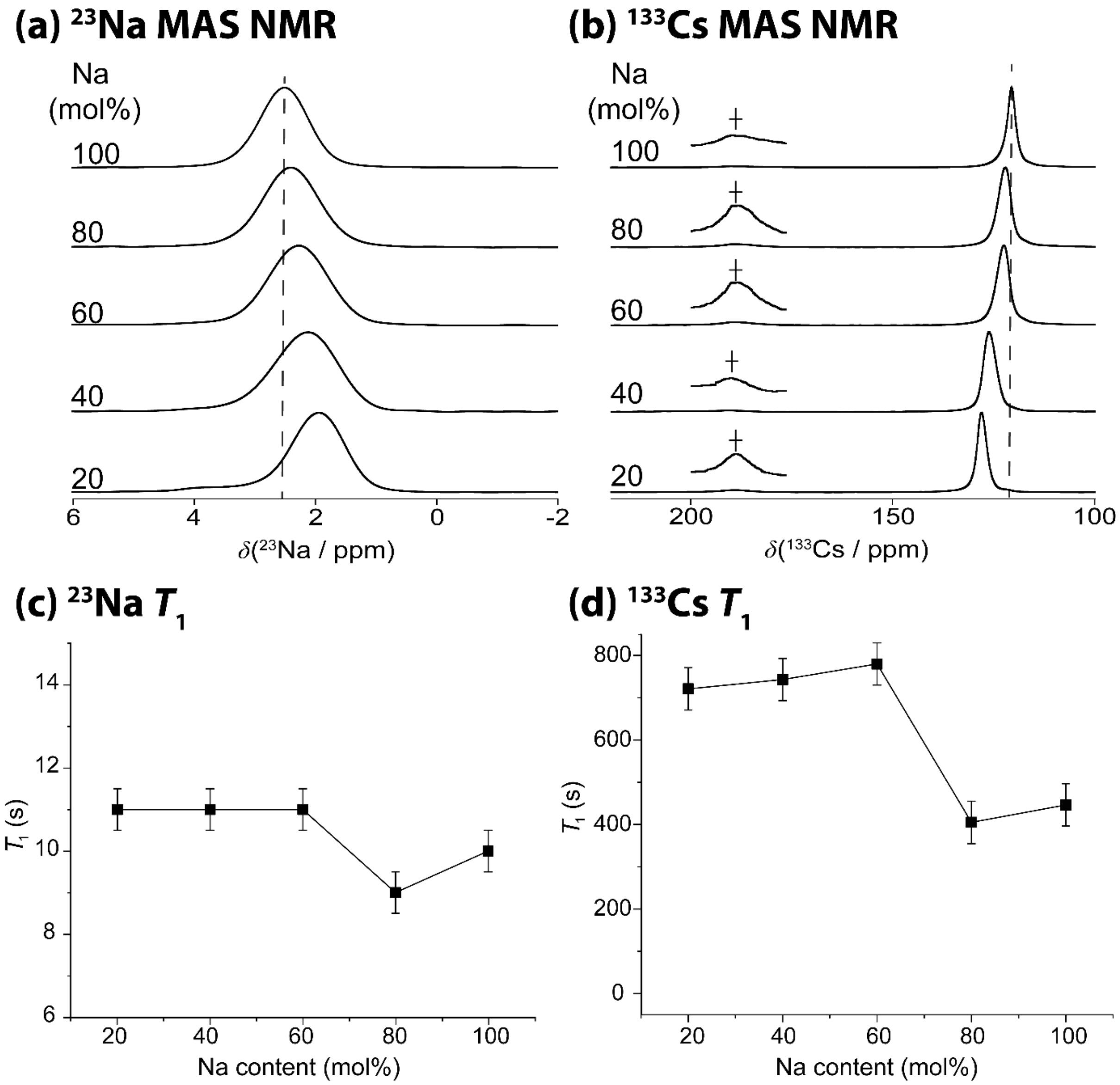

Figure 4. Solid state NMR study of the $Cs_2Na_xAg_{1-x}InCl_6$:Bi (x = 0.2 - 1) nanocrystal series showing (a) ^{23}Na MAS NMR data (B_0 = 14.1 T, ν_r = 12 kHz), (b) ^{133}Cs MAS NMR data (B_0 = 14.1 T, ν_r = 12 kHz), (c) ^{23}Na T_1 data, and (d) ^{133}Cs T_1 data. The T_1 data was acquired using the saturation-recovery technique. The low-intensity resonance in the ^{133}Cs MAS NMR data at δ ~190 ppm denoted with a '†' indicates the presence of a minor $CsInCl_4$ impurity.

Figure 5 shows the absorption and PL data obtained from the $Cs_2Na_xAg_{1-x}InCl_6$:Bi (x = 0.2 - 1) nanocrystal series. A blue shift in absorption peak from 370 nm to 324 nm is observed as the Na^+ content increases from 0 - 100 mol%. It has been established that Na does not contribute to the valence band minima or conduction band maxima of the double perovskite band gap,[33] hence only minute changes in the PL characteristics are observed with changing in Na content (see Figure 5b). From Figure 5b it is clear that Na doping enhances the emission in these nanocrystals; this phenomenon has been previously reported for the bulk perovskite.[39] Luo *et al.* revealed that the increase in PLQY is due to the break in inversion symmetry of $Cs_2AgInCl_6$ by creating $NaCl_6$ octahedra, allowing electron-hole overlap and subsequent radiative recombination.[39] The emission mechanism is attributed to previously reported self-trapped exciton (STE) phenomena originating from Jahn-Teller distortion of $[AgCl_6]^{5-}$ octahedra in the excited state.[25, 39, 40] Figure 5b shows that the 100 mol% Na sample is not emissive, whereas the 60 mol% Na and 40 mol% Na demonstrated the highest PLQY values of 21% and 16%, respectively. A decrease in the PLQY for nanocrystals with compositions accommodating >60 mol% Na is attributed to onset of significant Cs vacancy formation and greater Cs^+ mobility (see Table S4) which directly correlates with a significant decrease in the ^{133}Cs T_1 of ~300 s depicted in Figure 4d. These vacancies in the crystal structure can cause non-radiative transitions through phonon emission which are dominant in both the 80 mol% Na and 100 mol% Na nanocrystal systems.

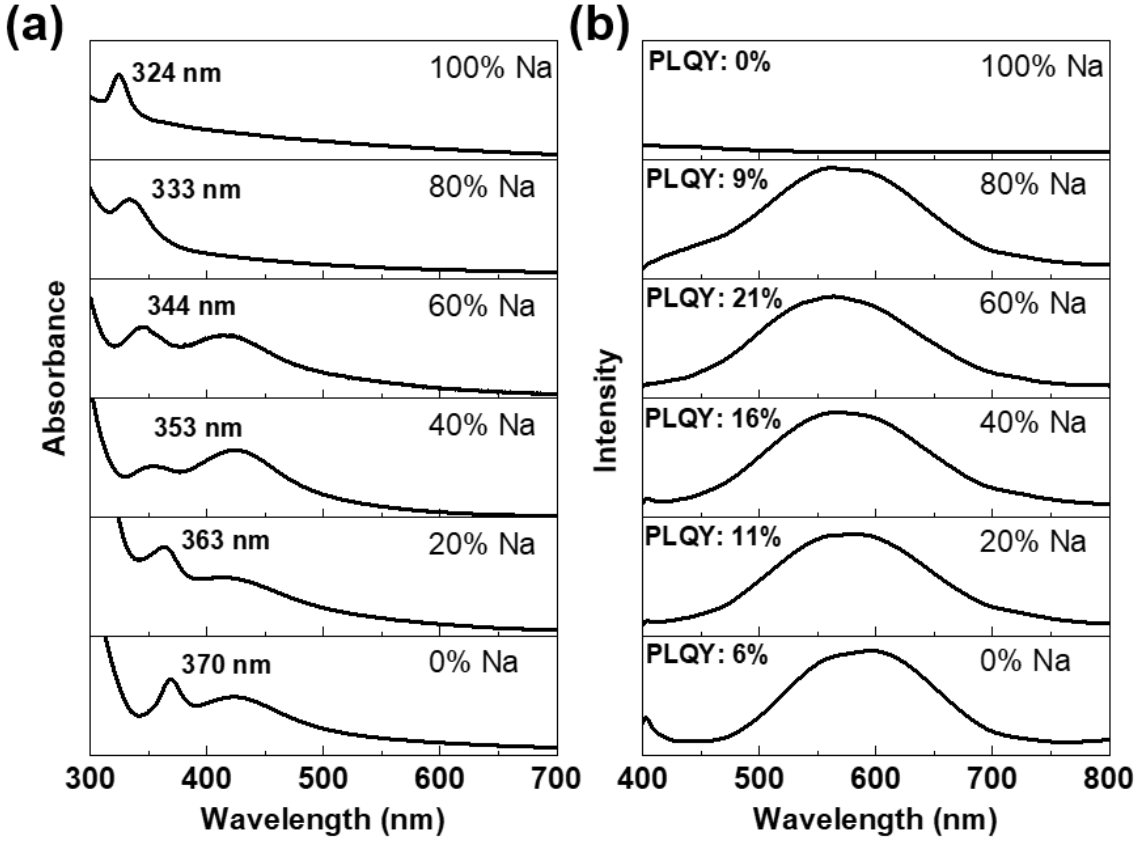

Figure 5. The (a) absorption, and (b) photoluminescence (PL) data from the $Cs_2Na_xAg_{1-x}InCl_6$:Bi (x = 0 - 1) nanocrystal series dispersed in hexane. The photoluminescence quantum yield (PLQY) is labelled in each spectrum.

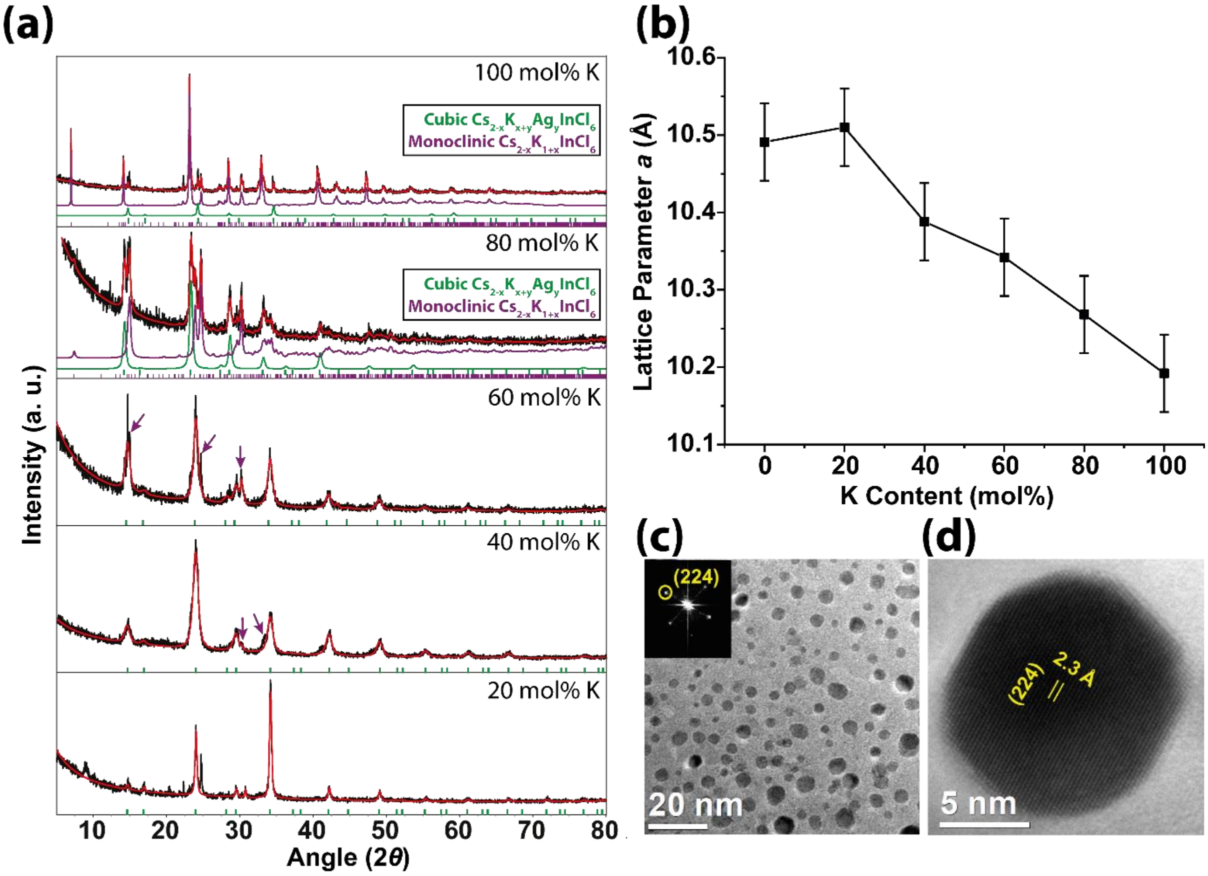

Figure 6. Structural characterisation data from the $Cs_2K_xAg_{1-x}InCl_6$:Bi (x = 0.2 - 1) nanocrystal series including, (a) powder XRD data with the arrows in the 40 mol% K and 60 mol% K diffraction patterns indicating the onset of a monoclinic phase(s), (b) changes to the cubic lattice parameter *a* with increasing mol% K, (c) TEM micrograph of $Cs_2K_{0.60}Ag_{0.40}InCl_6$:Bi nanocrystals with FFT, and (d) a HRTEM image of a $Cs_2K_{0.60}Ag_{0.40}InCl_6$:Bi nanocrystal depicting lattice fringes of associated with the cubic components of the overall structure.

$Cs_2K_xAg_{1-x}InCl_6$:Bi (x = 0 - 1) Nanocrystal System

Although Na^+ incorporation into the double perovskite system improves the optical and structural properties, other B'(I) possible cation substitutions can be realised to create alloys. Due to its compatible ionic radius, the K^+ cation can be considered as a viable candidate for incorporation into the $Cs_2AgInCl_6$:Bi framework on the Ag^+ position. A K^+-substituted compositional series of the form of $Cs_2K_xAg_{1-x}InCl_6$:Bi (x = 0.2 - 1) was synthesized with a stoichiometry mirroring the Na^+ series. In comparison to the $Cs_2In_xBi_{1-x}AgCl_6$ (x = 0 - 1) and the $Cs_2Na_xAg_{1-x}InCl_6$:Bi (x = 0.2 - 1) nanocrystal series which represent direct substitutional systems, the powder XRD data of Figure 6 and the ^{133}Cs and ^{39}K MAS NMR data of Figure 7 demonstrate that the $Cs_2K_xAg_{1-x}InCl_6$:Bi (x = 0.2 - 1) system is more complex where the formation of other similar phases competes for components of the K^+ inventory.

The powder XRD data of Figures 6a and S6 characterising the $Cs_2K_xAg_{1-x}InCl_6$:Bi (x = 0.2 - 1) nanocrystal series are refined as two similar crystal types consisting of a cubic perovskite phase (space group $Fm\bar{3}m$) and a monoclinic phase similar to the CsK_2BiCl_6 (space group $C12/c1$)[52] or $Cs_{2-x}K_{1+x}InCl_6$ (space group $C2/c$) structure types.[53] The appearance of reflections at 29° and 34° 2θ in the 40 mol% K (see Figure 6a) indicate the onset of a monoclinic phase; this phase assumes greater prominence with increasing mol% K^+ (particularly at the 80 and 100 mol% K^+ levels). Furthermore, Figure 6b also shows that the cubic perovskite $Fm\bar{3}m$ phase is described by a decreasing a lattice parameter with increasing mol% K^+. As the ionic radius of K^+ (1.38 Å) is larger than Ag^+ (1.15 Å), the a lattice parameter of this cubic phase is expected to increase proportionally with K content as per Vegard's law.[54] However, Figure 6b demonstrates that the lattice parameter a decreases as the 20 mol% K level is exceeded, suggesting that the K^+ cation is incorporated on both the Cs^+ (A) and Ag^+ (B'(I)) sites in this cubic structure. The TEM micrographs of the $Cs_2K_{0.60}Ag_{0.40}InCl_6$:Bi and $Cs_2K_{0.40}Ag_{0.60}InCl_6$:Bi nanocrystals in Figures 6c and S1 reveal faceted particles of ~4 nm and

~6 nm diameter, respectively, while the HRTEM micrograph of Figures 6d exhibit the lattice fringes and lattice spacing of 2.3 Å representing the (224) crystal plane associated with the cubic double perovskite structure. The smaller particle size characterising the K^+ substituted nanocrystals is attributed to the comparatively slower reaction dynamics in the synthesis mixture.

From the TEM images of Figures 6c and d, and SI1c, the small nanocrystal size of ~4 - 6 nm characterising the $Cs_2K_xAg_{1-x}InCl_6$:Bi (x = 0.2 - 1) series induces lower resolution XRD data (see Figures in 6a and S6). While the XRD data provides indications of the structural polytypes formed throughput this series, the short range information afforded by the solid state ^{133}Cs and ^{39}K MAS NMR data (see Figures 7a-d), and the associated AIRSS materials modelling provide greater specificity to the evolving phases stimulated by the changing stoichiometry. As observed in Scheme 1, based on varying amounts of K^+ cation substitution into the parent $Cs_2AgInCl_6$ structure,[34] a broad range of crystalline structures were generated that exhibited considerable differences in the rigidity of the perovskite framework. In all these substituted systems, AIRSS modelling initiated a series of random $InCl_6$ octahedra rotations and geometry relaxations to arrive at structural realisations representing lower energies in the potential energy surface than the original $Fm\bar{3}m$ structure. From Scheme 1 the resultant families of cubic and monoclinic crystalline structures accommodate various degrees of octahedral tilting and distortion within each lattice. The parent structure $Cs_2AgInCl_6$ was found to be the most rigid, with the perfect $Fm\bar{3}m$ structure defined as the ground state in these relaxation experiments. Substituting Cs^+ atoms for K^+ on the A site results in distorted structures that are energetically more favourable than the perfect cubic crystal, although the energy differences are not more than 15 meV/formula unit, thus indicating a flat potential energy landscape where the $InCl_6$

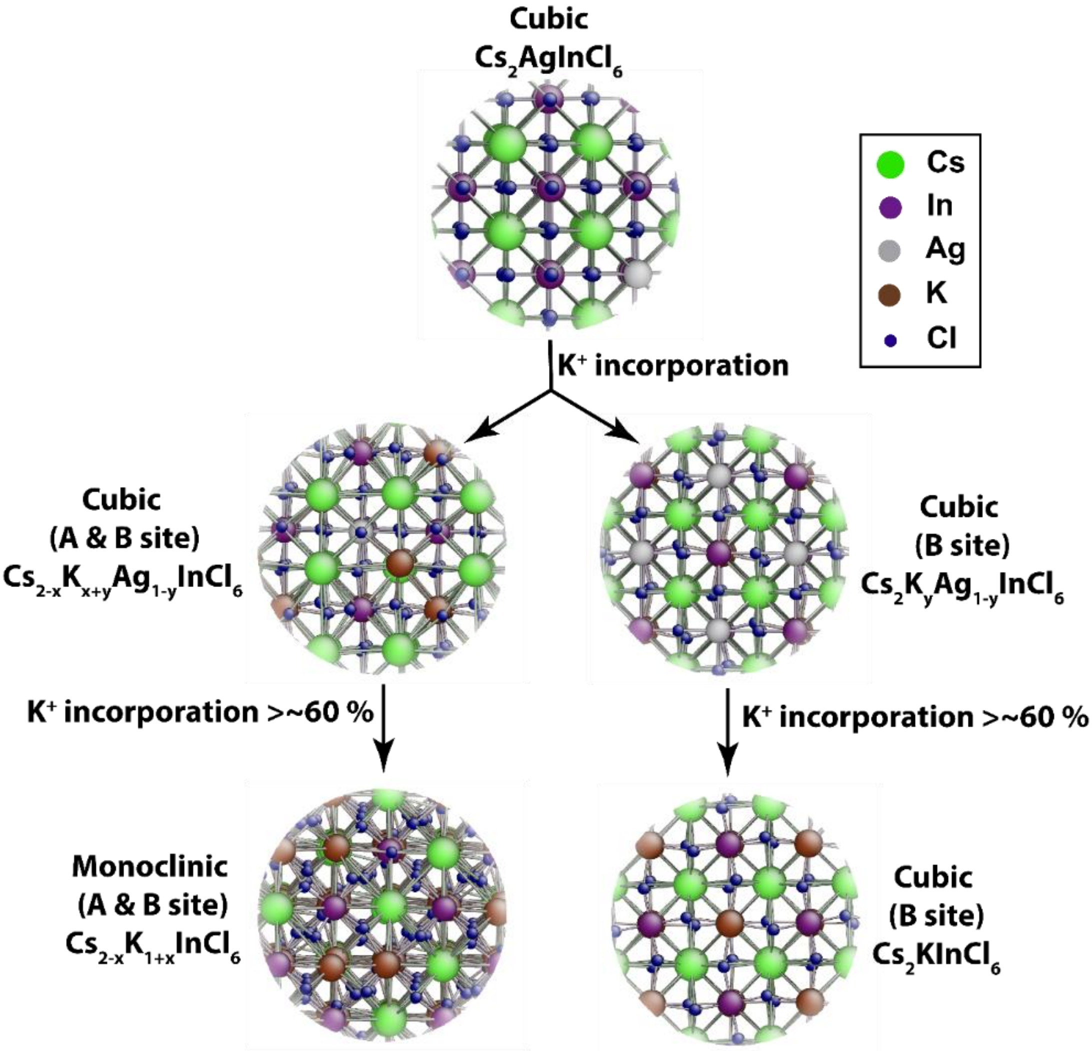

Scheme 1

octahedra have considerable rotational flexibility at finite temperatures. This phenomenon is emphasised upon inspection of the relaxed monoclinic $Cs_{2-x}K_{1+x}InCl_6$ structure (A and B site K^+ occupancy) which exhibits significant long-range disorder while preserving the overall local pseudo-cubic structure of the metal cations, thus corroborating the XRD data reported above.

The partial density of states (DoS) calculated from the AIRSS generated structures shown in Scheme 1 are presented in Figures 7a-f. From the evolution of the B site substituted cubic structures with increasing K^+ incorporation depicted on the right side of Scheme 1, the calculated DoS progressing from the parent $Cs_2AgInCl_6$ system, to the partially substituted $Cs_2K_yAg_{1-y}InCl_6$ (B site occupancy, y = 0.5) through to the fully substituted Cs_2KInCl_6 (B site occupancy, y = 1) reveals a reduction and an eventual loss of covalent bonding character between the anionic Cl^- and the $B(I)^+$ cations upon K^+ incorporation (see Figures 7a-c). This rationalises the increased flexibility and ionic character of the system with increasing mol% K^+ by highlighting that the isoenergetic relationship between the Cl^- *p* electrons and the Ag^+ *d* electrons (spanning ~1.5 - 4.5 eV) underpinning $Cs_2AgInCl_6$ is replaced by a large energy displacement between the Cl^- *p* electrons and the K^+ *p* electrons in Cs_2KInCl_6 of ~10 eV. Similarly, the DoS for the evolution of the A and B site substituted systems on the left side of Scheme 1 to the cubic $Cs_{2-x}K_{x+y}Ag_{1-y}InCl_6$ and eventually the monoclinic $Cs_{2-x}K_{1+x}InCl_6$ systems (see Figures 7e and f) reflects the same loss of covalency and structural rigidity.

Calculation of the lattice parameters from the generalised cubic $Cs_{2-x}K_{x+y}Ag_{1-y}InCl_6$ AIRSS realisation demonstrates that K^+ substitution can be partitioned in two competing scenarios (see Figure 7g). The lattice parameter changes from both A and B site substitution are represented as change to the average edge length of the (pseudo)cubic sublattice for monoclinic and cubic realisations of $Cs_{2-x}K_{x+y}Ag_{1-y}InCl_6$. Observation of the orange curves show that by keeping the B site occupancy constant (i.e. y = 0.0, 0.5, 1.0) and varying the A site substitution, the lattice contracts in agreement with the XRD data of Figures 6a and b. This contraction is accompanied by structural distortion which ultimately destabilises the cubic structure at high A site substitution levels. Conversely, the blue curves demonstrate that by keeping the A site occupancy constant (i.e. x = 0.0, 0.5) B site variation induces lattice expansion.

The ^{133}Cs and ^{39}K MAS NMR data measured from the $Cs_2K_xAg_{1-x}InCl_6$:Bi (x = 0.2 - 1) nanocrystal series is shown in in Figures 8a and b, while assignment of these complex spectra is assisted by GIPAW DFT calculation of the chemical shift distributions calculated from the AIRSS modelled structures of Scheme 1 (see Figures 8c and d). An important feature to note from both the ^{133}Cs and ^{39}K MAS NMR data is that the parent cubic $Cs_2AgInCl_6$ and cubic (B site substituted) $Cs_2K_yAg_{1-y}InCl_6$ structures exhibit confined chemical shifts ranges at δ ~128 ppm and δ ~50 ppm, respectively, while all other systems display marked chemical shift distributions commensurate with the structural disorder defining the less rigid/more ionic systems. From the ^{133}Cs MAS NMR data in Figure 8a, the lower substitution levels of 20 - 60 mol% K^+ are dominated by the cubic (B site substituted) $Cs_2K_yAg_{1-y}InCl_6$ species, although evidence of the cubic (A and B site substituted) $Cs_{2-x}K_{x+y}Ag_{1-y}InCl_6$ and cubic (A site substituted) $Cs_{2-x}K_xAgInCl_6$ systems is observed to emerge. Figures 8a and c demonstrate that the substitution of K^+ onto the Cs^+ A site introduces significant structural disorder as reflected by the large GIPAW DFT predicted chemical shift dispersion spanning ~80 - 100 ppm. The clearest experimental evidence of these disordered species is via the very broad, partially resolved (bimodal) resonance distributions centred at δ ~150 ppm and δ ~120 ppm (see Figure 7c). At the higher 80 and 100 mol% K^+ substitution levels the rigid/covalent cubic (B site substituted) $Cs_2K_yAg_{1-y}InCl_6$ structure disappears and the speciation is dominated by the less rigid/more ionic cubic (B site substituted) Cs_2KInCl_6 and monoclinic (A and B site substituted) $Cs_{2-x}K_{1+x}InCl_6$ systems, in addition to the cubic (A and B site substituted) $Cs_{2-x}K_{x+y}Ag_{1-y}InCl_6$ and (A site substituted) $Cs_{2-x}K_xAgInCl_6$ systems mentioned above. The newly emergent cubic (B site substituted) Cs_2KInCl_6 and monoclinic (A and B site substituted) $Cs_{2-x}K_{1+x}InCl_6$ systems are also characterised by complex disorder and broad predicted chemical shift ranges of ~50 ppm and ~80 ppm, respectively, which are thus partially resolved in the experimental data.

Unlike the Cs^+ cation which only occupies the A site in this series of structures, the incorporation of the K^+ cation on both the A and B positions introduces more profound affects to the observed ^{39}K MAS NMR data of Figure 8b. The A site and B site ^{39}K shifts are partitioned into distinctly resolved chemical shift ranges, with the K speciation occupying the cubooctahedral A sites displaying ^{39}K shifts in the δ ~–50 - 20 ppm range, while the octahedral B site substitution is comparatively less shielded exhibiting ^{39}K shifts in the δ ~50 - 80 ppm range. The component of the K inventory entering the rigid cubic $Cs_2K_yAg_{1-y}InCl_6$ structure (B site occupancy) is confined to a very narrow ^{39}K chemical shift range around δ ~50 ppm. It is important to note that the lower level (20 mol% K^+) of incorporation does not introduce K^+ cation speciation into B site of the cubic $Cs_2K_yAg_{1-y}InCl_6$ system; i.e. there is no evidence of a narrow resonance at δ ~48 ppm, however, a broad distributed resonance centred around δ ~20 ppm is observed. According to the GIPAW DFT calculated ^{39}K chemical shift ranges of Figure 8d, the K speciation delivered at the 20 mol% K^+ incorporation level is distributed throughout disordered cubic (A site substituted) $Cs_{2-x}K_xAgInCl_6$ and (A and B site substituted) $Cs_{2-x}K_{x+y}Ag_{1-y}InCl_6$ phases. This represents a surface passivation phenomenon of the parent cubic $Cs_2AgInCl_6$ nanocrystals, with the corresponding (narrow) ^{133}Cs MAS NMR resonance of the 20 mol% K^+ system representing the Cs speciation comprising the $Cs_2AgInCl_6$ nanocrystal bulk. Despite the low signal/noise of the ^{39}K MAS NMR data from the lower 20 and 40 mol% K^+ incorporation levels, the absence of bimodal ^{39}K chemical shift distributions suggests that a cubic (A site substituted) $Cs_{2-x}K_xAgInCl_6$ phase dominates the surface K passivation. This observation is consistent with recent reports of the surface passivation of $Cs_2AgInCl_6$ and $CsIn_{0.9}Bi_{0.1}AgCl_6$ nanocrystals using low levels of K^+ cations introduced as KBr.[55] The GIPAW DFT calculated ^{39}K chemical shift distributions shown in Figures 8d suggest that significant overlap influences both the A and B site shift ranges, precluding chemical resolution of the constituent cubic and monoclinic phases in each case. However, more importantly, the distinct resolution between the A and B site chemical shift ranges demonstrates that the K^+ substitution levels into this nanocrystal series (particularly at the higher incorporation levels) is dominated by A site occupancy by a factor of ~2.5 - 4.0 (see Table S5).

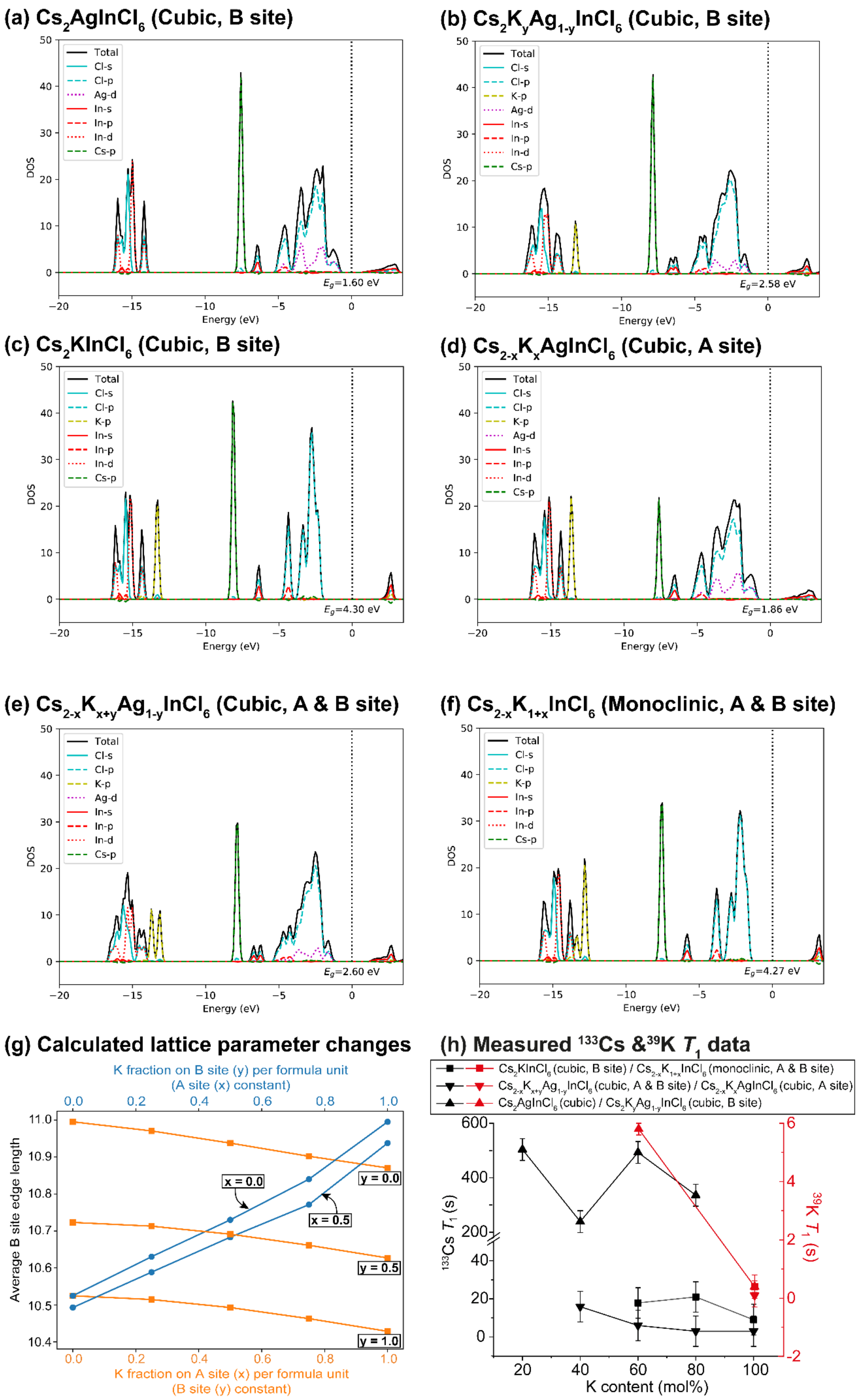

Figure 7. The calculated partial density of states (DoS) for (a) cubic $Cs_2AgInCl_6$, (b) cubic (B site substituted) $Cs_2K_yAg_{1-y}InCl_6$ (y = 0.5), (c) cubic (fully B site substituted) Cs_2KInCl_6, (d) to cubic (A site substituted) $Cs_{2-x}K_xAgInCl_6$ (x = 0.5), (e) cubic (A and B site substituted) $Cs_{2-x}K_{x+y}Ag_{1-y}InCl_6$ (x = 0.5, y = 0.5), (f) monoclinic (A and B site substituted) $Cs_{2-x}K_{1+x}InCl_6$ (x = 0.25), with (g) the calculated lattice parameter changes and (h) the measured ^{133}Cs and ^{39}K T_1 data acquired using the saturation-recovery technique.

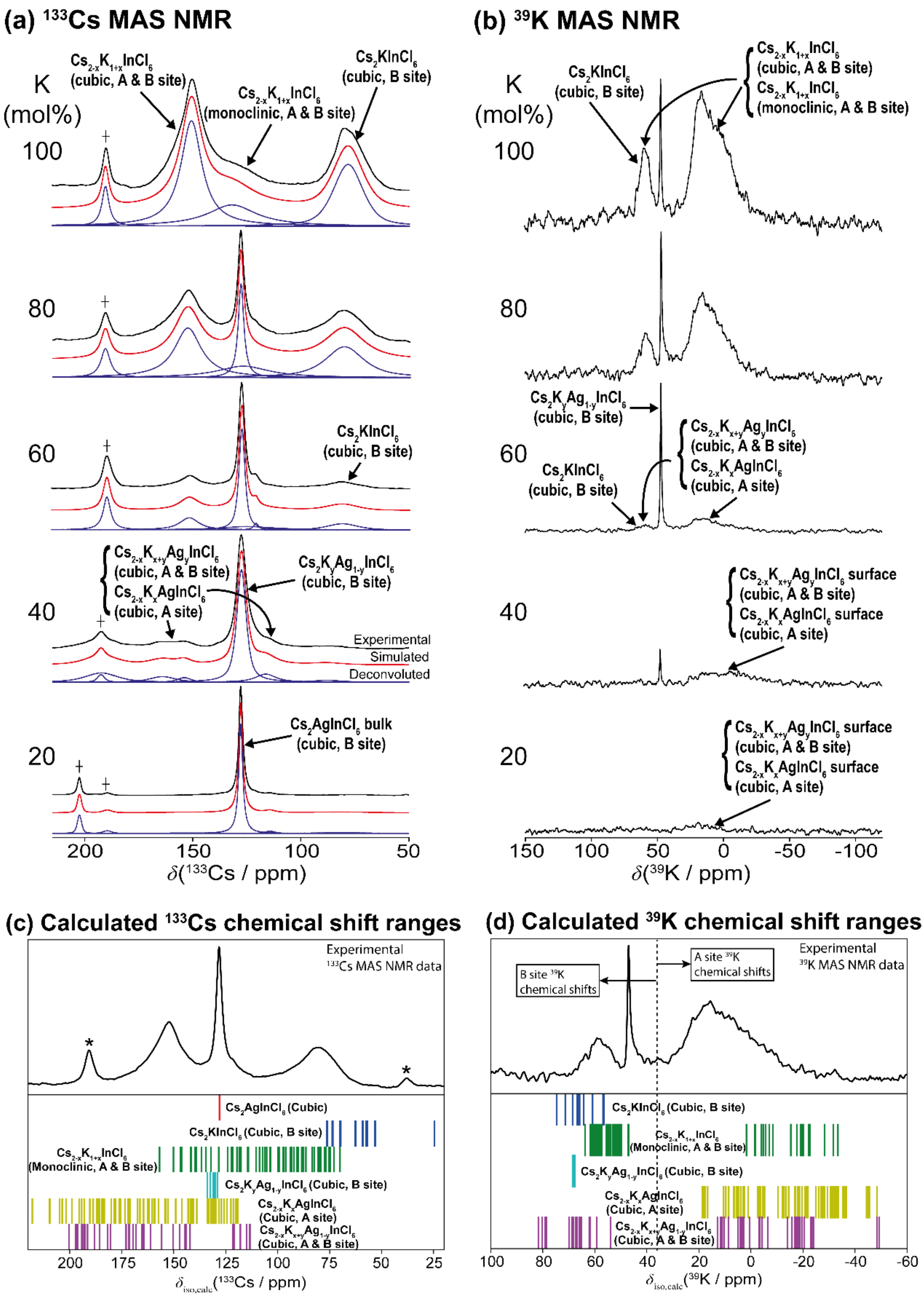

Figure 8. Solid state NMR study of the $Cs_2K_xAg_{1-x}InCl_6$:Bi (x = 0.2 - 1) nanocrystal series showing (a) ^{133}Cs MAS NMR data (B_0 = 14.1 T, ν_r = 12 kHz), (b) ^{39}K MAS NMR data (B_0 = 20.0 T, ν_r = 12 kHz), (c) the GIPAW DFT calculated ^{133}Cs chemical shift ranges (for various levels of K^+ substitution), and (d) the GIPAW DFT calculated ^{39}K chemical shift ranges (for various levels of K^+ substitution).

Despite the large ^{133}Cs and ^{39}K linewidths and lack of resolution that characterises the structural disorder within K^+ substituted nanocrystal series, valuable information can be obtained from the T_1 relaxation data from those resonances that can be isolated. From the ^{133}Cs MAS NMR data three distinct resonances at δ ~128 ppm (cubic (B site substituted) $Cs_2AgInCl_6$/$Cs_2K_yAg_{1-y}InCl_6$ phases), δ ~152 ppm (convoluted cubic (A site substituted) $Cs_{2-x}K_xAgInCl_6$ and cubic (A and B site substituted) $Cs_{2-x}K_{x+y}Ag_{1-y}InCl_6$ phases) and, δ ~82 ppm (convoluted cubic (fully B site substituted) Cs_2KInCl_6 and monoclinic (A and B site substituted) $Cs_{2-x}K_{1+x}InCl_6$ phases) exhibit sufficient resolution for a T_1 relaxation analysis. The measured ^{133}Cs T_1 relaxation data is reported as a function of mol% K^+ incorporation in Figure 7h and Table S4. These data highlight differences of over two orders of magnitude exists between the ^{133}Cs T_1s characterising the rigid (cubic (B site substituted) $Cs_2AgInCl_6$/$Cs_2K_yAg_{1-y}InCl_6$ phases, T_1s of ~250 - 500 s) and the more disordered and flexible structures represented by broader resonance linewidths (T_1s of ~5 - 20 s), thus corroborating the DoS data presented in Figures 7a-f. Figure 8h displays a noticeable decrease in the ^{133}Cs T_1s at the 40 mol% K^+ incorporation level. As the 20 mol% K incorporation level probably only represents a surface passivation event (see the ^{39}K MAS NMR data above), the T_1 measurement of ~500 s from this sample represents Cs^+ cations in the bulk $Cs_2AgInCl_6$ structure. Hence, the reduced T_1 of ~250 s at 40 mol% K represents the initial K^+ cation introduction into the $Cs_2AgInCl_6$ framework, which is probably distributed inhomogeneously throughout quasi-stable surface, sub-surface and near-surface environments of the nanocrystal (see the ^{39}K MAS NMR data of Figure 8b). As evidenced by the ^{39}K MAS NMR data of the 60 mol% K preparation, the increase of the ^{133}Cs T_1 back to ~500 s is accompanied by the maximum proliferation of K^+ into the bulk $Cs_2AgInCl_6$ framework (producing the B site substituted $Cs_2K_yAg_{1-y}InCl_6$ phase), suggesting that the substituted $Cs_2K_{0.60}Ag_{0.40}InCl_6$ phase represents an important balance between covalent character, restricted Cs^+ mobility and K^+ incorporation (see Figure 8b).9 and

Figures 9a and 9b show the absorption and emission data from the $Cs_2K_xAg_{1-x}InCl_6$:Bi (x = 0.2 - 1) nanocrystal series. From Figure 9a, a blue shift in the excitonic peak spanning 370 nm to 328 nm is observed across this compositional range; however, there is no apparent shift in the PL peak as K^+ cations do not perturb the valence band maxima or conduction band minima of the double perovskite band gap (see Figure 9b).[33] Figure 9c shows the relative PL performance from the $Cs_2AgIn_{0.90}Bi_{0.10}Cl_6$, $Cs_2Na_{0.60}Ag_{0.40}InCl_6$:Bi, and $Cs_2K_{0.60}Ag_{0.40}InCl_6$:Bi nanocrystal samples that present the highest PLQY within each compositional series, demonstrating that the K^+ substituted $Cs_2K_{0.60}Ag_{0.40}InCl_6$:Bi nanocrystals represent the best performing systems by a factor of ~100%. More importantly, Figure 9d indicates that K^+ incorporation induces significant improvements to the optical properties specifically at the 60 mol% K level where the PLQY increases from 38%. Indeed, Figures 9d and e show that the increasing PLQY performance of the K^+ substituted series correlates directly with amount of the cubic (B site substituted) $Cs_2K_yAg_{1-y}InCl_6$ phase present which is maximized at the 60 mol% K level. Although the XRD, MAS NMR and materials modelling studies reveal that compositions supporting >20 mol% K accommodate simultaneous K^+ substitution on both the A (Cs) and B'(I) (Ag) double perovskite positions, Figures 9d and e emphasize that the 60 mol% K preparation optimises the presence of the cubic (B site substituted) $Cs_2K_yAg_{1-y}InCl_6$ phase that shows the most effective passivation of the Cs^+ bulk and surface defects as indicated by the longest ^{133}C and ^{39}K T_1 values (see Figure 7h), attenuated cation mobility and enhanced PLQY performance. From the XRD data of Figures 6a and S6, and the ^{133}Cs and ^{39}K MAS NMR of Figures 8a and b, respectively, increased K^+ incorporation of >60 mol% K induces the formation of large quantities of disordered cubic and monoclinic phases where A site substitution dominates the K speciation. These less rigid/more ionic phases are characterised by greatly reduced T_1s, increased cation mobility and much reduced PLQY function.

It is important to note that a direct observation of the optical band gaps in these types of materials are difficult to observe experimentally. As discussed in Reference 35, this is a consequence of the transitions between the valence band maximum to the conduction band minimum being parity forbidden. The complexity of these processes is highlighted by the theoretically calculated and measured data presented in the manuscript Figures 1f,g, 5a,b, 7a-f, and 9a,b, and in Figure S9 and Table S6 within the SI. A qualitative estimate from the PLQY data for all nanocrystal systems in this study places most band gaps in the ~1.5 - 2.2 eV range which is in reasonable agreement with the band gap values elucidated from the first principles band structure/DoS calculations presented in Figure 7. Similarly, the calculated absorption spectra for $Cs_2AgInCl_6$ and $Cs_2AgBiCl_6$ nanocrystal systems shown in Figure S6, also determined from first principles band structure data, semi-quantitatively corroborates the experimentally measured absorption data from these materials (see top and bottom spectra from Figure 1f). However, this contrasts with the Tauc plot estimation of the band gaps for all UV/vis absorption spectra as presented in Table S6 which, (a) demonstrate minor variation with composition, and (b) represent a significant overestimation in comparison to the calculated results. For the Tauc plot estimations, the band gap is calculated using a direct band gap of these materials as the actual fundamental band gap is more complex as it is comprised of parity forbidden direct and indirect transition processes. Although emission transitions are not necessarily prevented, the excited electron-hole pair may have a long lifetime thus affecting the efficiency of the emission. It is assumed the introduction of structural disorder and symmetry reduction partially allows parity-forbidden transitions, thereby increasing the overall PL efficiency in both absorption and emission modes.

Similar improvements to the optical properties by surface passivation have been reported from the incorporation of K^+ cations into other ABX_3 perovskite systems.[56] It is important to note that a measured PLQY of 38% for the 60 mol% K system represents a maximum theoretical threshold as the uncoordinated Cl^- ions on the nanocrystals surface limit the emission efficiency in double perovskite structure.[57] While further developments are necessary to improve the PLQY in these nanocrystal systems, this XRD/MAS NMR/materials modelling approach has demonstrated that K^+ cation incorporation induces the evolution of multiple phases associated with simultaneous A and B site passivation. Furthermore, the K^+ cation substitution series shows a clear dominance of the A site substitution phenomenon (particularly at the higher incorporation levels); however, the PLQY performance is optimised when the maximum amounts of the cubic (B site substituted) $Cs_2K_yAg_{1-y}InCl_6$ phase comprises the nanocrystal structure. Hence, clearly beneficial developments in this nanocrystalline double perovskite material system would involve increased relative yields (or complete dominance) of the $Cs_2K_yAg_{1-y}InCl_6$ phase.

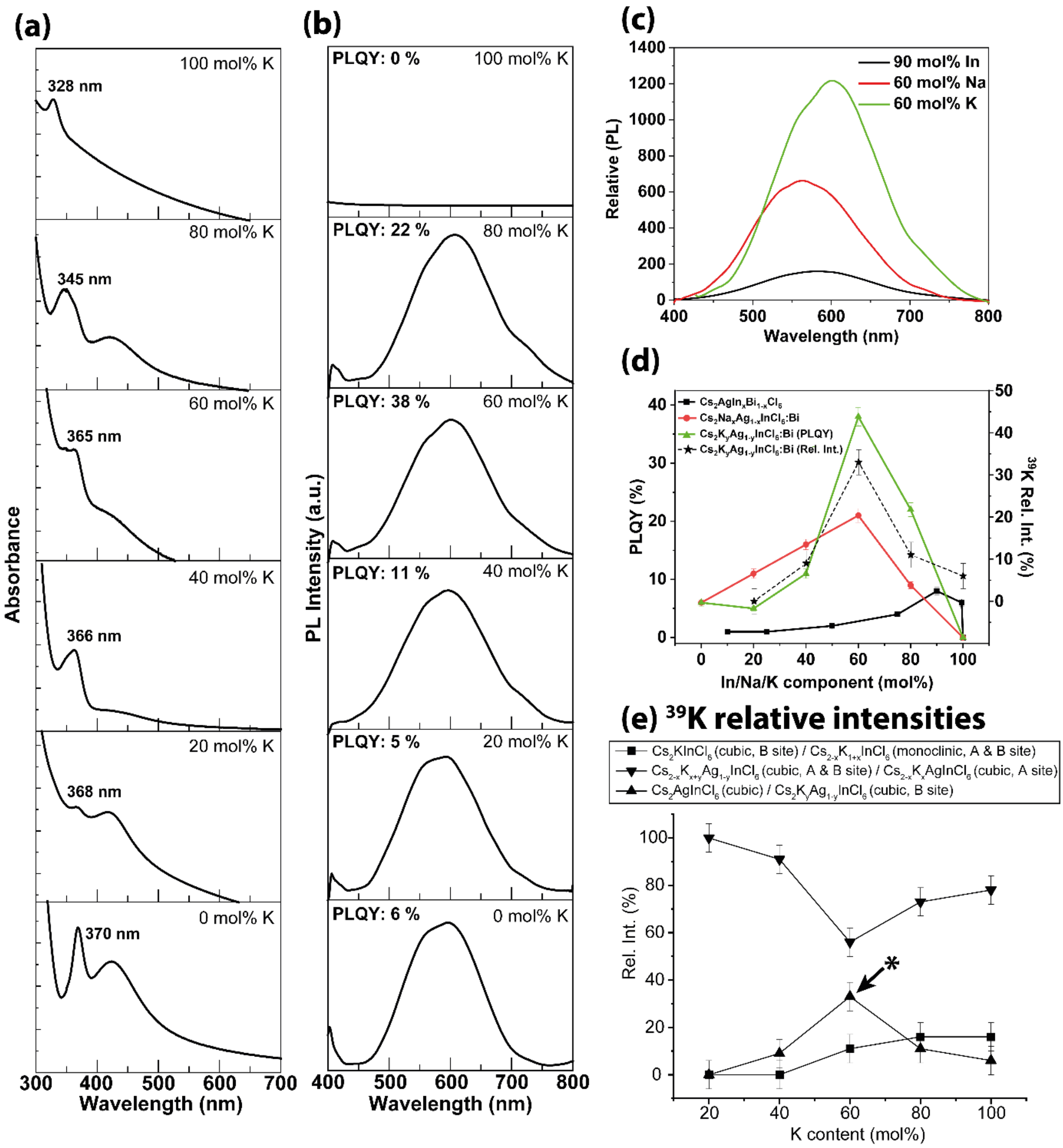

Figure 9. Optoelectronic data from the $Cs_2K_xAg_{1-x}InCl_6$:Bi (x = 0 - 1) nanocrystal series displaying (a) absorption spectra and (b) photoluminescence (PL) spectra from nanocrystal solutions dispersed in hexane, (c) the relative PL data from the $Cs_2AgIn_{0.90}Bi_{0.10}Cl_6$, $Cs_2Na_{0.60}Ag_{0.40}InCl_6$:Bi, and $Cs_2K_{0.60}Ag_{0.40}InCl_6$:Bi systems yielding the highest PLQY in each nanocrystal series, (d) the trend in PLQY vs mol% Na/mol% K/mol% In, and (e) the relative intensity of the K speciation measured from the ^{39}K MAS NMR data. The PLQY behaviour demonstrated by the K substituted series in (d) directly correlates with the amount of cubic $Cs_2K_yAg_{1-y}In_xCl_6$ phase represented by the δ 48 ppm resonance from the ^{39}K MAS NMR data in (e) and in Figure 7b (maximum indicated with an asterisk *).

Conclusion

Three series of nanocrystals samples, $Cs_2In_xBi_{1-x}AgCl_6$, $Cs_2Na_xAg_{1-x}InCl_6$:Bi, and $Cs_2K_xAg_{1-x}InCl_6$:Bi, were synthesised using a colloidal hot-injection procedure. $Cs_2AgIn_xBi_{1-x}Cl_6$ nanocrystals were synthesised as a baseline system, with the 0.5% Bi doped sample ($Cs_2AgInCl_6$:Bi) being taken forward for investigations of the Na^+ and K^+ cation incorporation into these double perovskite nanocrystalline materials. A combined XRD, TEM and solid state MAS NMR approach demonstrated that clear structural and functional trends were observed for the $Cs_2In_xBi_{1-x}AgCl_6$ (x = 0 - 1) and $Cs_2Na_xAg_{1-x}InCl_6$:Bi (x = 0 - 1) substitutional series. The $Cs_2In_xBi_{1-x}AgCl_6$ (x = 0 - 1) series exhibited ^{133}Cs T_1 values that are 2 - 3 orders of magnitude greater than the those representing the mid-range ~50 mol% In^{3+} compositions thus reflecting increased Cs^+ mobility where maximum structural disorder is present. In contrast, the maximum measured ^{133}Cs T_1 values were evident for compositions close to (but not directly at) the end member $Cs_2BiAgCl_6$ and $Cs_2InAgCl_6$ compositions, suggesting that minor substituted amounts of In^{3+} in the $Cs_2BiAgCl_6$ system, and Bi^{3+} within the $Cs_2InAgCl_6$ system, induce marked passivation effects within this system. This phenomenon is highlighted by the strong orange emission at ~580 nm dominating the PL properties up to a composition of 99.5 mol% In^{3+}, but which subsequently disappears at 100 mol% In^{3+}.

The $Cs_2Na_xAg_{1-x}InCl_6$:Bi (x = 0 - 1) nanocrystal series highlights the complementary and interconnected roles that the cations such as Bi^{3+} and Na^+ adopt within this nanocrystalline framework. The larger and more highly charged Bi^{3+} cation is clearly essential for defect passivation which assists the attenuation of the Na^+ cation mobility up to the 60 mol% Na^+ incorporation level where a maximum PLQY of 21% is achieved. At higher Na^+ substitution levels (i.e. >60 mol% Na^+) the effectiveness of the Bi^{3+} cation passivation is decreased and a concomitant reduction in the Cs elemental ratio develops as detected by the TEM EDXS data (see Table S3). This facilitates increased Cs^+ vacancy formation and more rapid Cs^+ and Na^+ cation mobility as characterised by reduced ^{133}Cs and ^{23}Na T_1 relaxation times.

The $Cs_2K_xAg_{1-x}InCl_6$:Bi (x = 0 - 1) nanocrystal series behaves in similar fashion to its analogous alkali Na^+ series as the Bi^{3+} passivation helps to restrict K^+ mobility up to the 60 mol% K^+ level where a maximum PLQY of 38% is obtained. This performance represents a maximum theoretical threshold for these materials as the uncoordinated Cl^- ions on the nanocrystals surface limit the emission efficiency in double perovskite structure,[57] nevertheless it is highly suitable for optoelectronic applications including photovoltaic and light emitting devices. Once again, this behaviour is indicated by the ^{39}K T_1 measurements that are maximised at this substitution level. However, in marked contrast to the Na^+ nanocrystal series, the smaller ionic radius of the K^+ cation also stimulates the formation of a complex array of competing, closely related K^+ substituted phases. XRD studies demonstrated that cubic and monoclinic phases co-exist in the nanocrystal structure, while solid state ^{133}Cs and ^{39}K MAS NMR studies, AIRSS materials modelling and GIPAW DFT chemical shift calculations verified the specific cubic and monoclinic phases present. All of these studies conclusively proved that K^+ incorporation in these nanocrystals can occur on both A and B'(I) positions of the double perovskite structure, and the DFT DoS calculations identified that varying degrees of covalent/ionic character and structural rigidity characterise the resultant phases. Optimum PL and PLQY behaviour were observed with maximum amounts of the structurally rigid 60 mol% K^+ $Cs_2K_yAg_{1-y}InCl_6$ phase that support B site occupancy, although the lower concentration preparations show clear evidence that the K^+ incorporation is initiated as surface passivation primarily on the A site. These findings involving K^+ substituted double perovskite $Cs_2InAgCl_6$ quantum dot systems have great implications, not only for optoelectronic and solar cell technologies, but also for the developing fields of photocatalytic CO_2 reduction and image sensor materials.[58,59]

Supporting Information

Experimental conditions for synthesis and characterization; additional TEM images and histograms for selected nanocrystal compositions; ^{133}Cs and ^{23}Na solid state MAS NMR data at two magnetic field strengths; table of NMR parameters and T_1s for each series; variation of T_1 and T_2 relaxation times under a dipolar mechanism; XRD patterns for $Cs_2Na_xAg_{1-x}InCl_6$:Bi, and $Cs_2K_xAg_{1-x}InCl_6$:Bi series; table showing the elemental analysis using EDXS; and ^{133}Cs and ^{39}K calibration curves for DFT calculated shieldings.

Author Contribution

PV designed the initial experiments related to the materials synthesis, while AJ, GVN and PV performed the material synthesis and characterization. BEG and JVH designed and performed all solid state NMR measurements, with YF and TW contributing to the crystallographic analysis. APB and JVH designed and implemented the materials modelling and DFT computational approaches. PV, BEG and JVH wrote the manuscript with all authors viewing and contributing to its content.

Acknowledgements

PV acknowledges a NTU Presidential Postdoctoral Fellowship, Singapore via grant 04INS000581C150OOE01. AJ acknowledges Prof. Superb Misra, IIT Gandhinagar for his support and facilitating the opportunity to work on this project. We acknowledge Prof. Nripan Mathews and Prof. Subodh G. Mhaisalkar (NTU, Singapore) for their valuable support, and Dr. Kai. Chen (Victoria University of Wellington, New Zealand) for his assistance with the optical analysis. JVH acknowledges financial support for the 400 MHz and 600 MHz solid state NMR instrumentation, and the UK High Field (850 MHz) Solid State NMR Facility, at Warwick used in this research which was funded by the EPSRC (grants EP/M028186/1 and EP/K024418/1), the BBSRC, the University of Warwick, and the Birmingham Science City AM1 and AM2 projects which were supported by Advantage West Midlands (AWM) and the European Regional Development Fund (ERDF). APB and JVH acknowledge the use of Athena at HPC Midlands+ which was funded by the EPSRC (Grant No. EP/P020232/1) as part of the HPC Midlands+ consortium, and acknowledge the University of Warwick Scientific Computing Research Technology Platform for assisting the research described within this study. JVH and TW also acknowledges the Centre of High Field NMR Spectroscopy and Imaging, and the Facility for Analysis, Characterization, Testing and Simulation (FACTS) at NTU, Singapore, for access to their solid state NMR, electron microscopy and X-ray diffraction facilities.

Conflicts of Interest

The authors declare that there are no conflicts of interest.

References

1. L. Protesescu, S. Yakunin, M. I. Bodnarchuk, F. Krieg, R. Caputo, C. H. Hendon, R. X. Yang, A. Walsh and M. V. Kovalenko, *Nano letters*, 2015, **15**, 3692-3696.
2. J. Butkus, P. Vashishtha, K. Chen, J. K. Gallaher, S. K. Prasad, D. Z. Metin, G. Laufersky, N. Gaston, J. E. Halpert and J. M. Hodgkiss, *Chemistry of Materials*, 2017, **29**, 3644-3652.
3. A. A. M. Brown, T. J. N. Hooper, S. A. Veldhuis, X. Y. Chin, A. Bruno, P. Vashishtha, J. N. Tey, L. Jiang, B. Damodaran and S. H. Pu, *Nanoscale*, 2019.
4. Y. Dong, Y.-K. Wang, F. Yuan, A. Johnston, Y. Liu, D. Ma, M.-J. Choi, B. Chen, M. Chekini and S.-W. Baek, *Nature Nanotechnology*, 2020, **15**, 668-674.
5. P. Vashishtha, B. E. Griffith, A. A. M. Brown, T. J. N. Hooper, Y. Fang, M. S. Ansari, A. Bruno, S. H. Pu, S. G. Mhaisalkar, T. White and J. V. Hanna, *ACS Applied Electronic Materials*, 2020, **2**, 4002–4011.
6. P. Vashishtha, S. A. Veldhuis, S. S. Dintakurti, N. L. Kelly, B. E. Griffith, A. A. Brown, M. S. Ansari, A. Bruno, N. Mathews,Y. Fang T. White, S. G. Mhaisalkar and J.V. Hanna, *Journal of Materials Chemistry C*, 2020, **8**, 11805-11821.
7. W. Van der Stam, J. J. Geuchies, T. Altantzis, K. H. Van Den Bos, J. D. Meeldijk, S. Van Aert, S. Bals, D. Vanmaekelbergh and C. de Mello Donega, *Journal of the American Chemical Society*, 2017, **139**, 4087-4097.
8. X. Y. Chin, A. Perumal, A. Bruno, N. Yantara, S. A. Veldhuis, L. Martínez-Sarti, B. Chandran, V. Chirvony, A. S.-Z. Lo and J. So, *Energy & Environmental Science*, 2018, **11**, 1770-1778.
9. J.-H. Wei, X.-D. Wang, J.-F. Liao and D.-B. Kuang, *ACS Applied Electronic Materials*, 2020.
10. F. Ambroz, W. Xu, S. Gadipelli, D. J. Brett, C. T. Lin, C. Contini, M. A. McLachlan, J. R. Durrant, I. P. Parkin and T. J. Macdonald, *Particle & Particle Systems Characterization*, 2020, **37**, 1900391.
11. H. Chen, L. Fan, R. Zhang, C. Bao, H. Zhao, W. Xiang, W. Liu, G. Niu, R. Guo and L. Zhang, *Advanced Optical Materials*, 2020, **8**, 1901390.
12. Y.-K. Wang, D. Ma, F. Yuan, K. Singh, J. M. Pina, A. Johnston, Y. Dong, C. Zhou, B. Chen and B. Sun, *Nature Communications*, 2020, **11**, 1-7.
13. W. Zheng, Q. Wan, Q. Zhang, M. Liu, C. Zhang, B. Wang, L. Kong and L. Li, *Nanoscale*, 2020, **12**, 8711-8719.
14. L. Xie, J. Chen, P. Vashishtha, X. Zhao, G. S. Shin, S. G. Mhaisalkar and N.-G. Park, *ACS Energy Letters*, 2019, **4**, 2192-2200.
15. Y. Ma, P. Vashishtha, K. Chen, E. L. Peach, D. Ohayon, J. M. Hodgkiss and J. E. Halpert, *ChemSusChem*, 2017, **10**, 2677-2684.
16. L. Xie, P. Vashishtha, T. M. Koh, P. C. Harikesh, N. F. Jamaludin, A. Bruno, T. J. Hooper, J. Li, Y. F. Ng and S. G. Mhaisalkar, *Advanced Materials*, 2020, 2003296.
17. M. Jeong, I. W. Choi, E. M. Go, Y. Cho, M. Kim, B. Lee, S. Jeong, Y. Jo, H. W. Choi and J. Lee, *Science*, 2020, **369**, 1615-1620.

18. H. Yang, Y. Zhang, J. Pan, J. Yin, O. M. Bakr and O. F. Mohammed, *Chemistry of Materials*, 2017, **29**, 8978-8982.
19. P. Vashishtha, S. Bishnoi, C. H. A. Li, M. Jagadeeswararao, T. J. N. Hooper, N. Lohia, S. B. Shivarudraiah, M. S. Ansari, S. N. Sharma and J. E. Halpert, *ACS Applied Electronic Materials*, 2020, DOI: 10.1021/acsaelm.0c00825.
20. R. X. Yang, J. M. Skelton, E. L. Da Silva, J. M. Frost and A. Walsh, *Journal of Physical Chemistry Letters*, 2017, **8**, 4720-4726.
21. A. A. Brown, B. Damodaran, L. Jiang, J. N. Tey, S. H. Pu, N. Mathews and S. G. Mhaisalkar, *Advanced Energy Materials*, 2020, **10**, 2001349.
22. T. C. Jellicoe, J. M. Richter, H. F. Glass, M. Tabachnyk, R. Brady, S. n. E. Dutton, A. Rao, R. H. Friend, D. Credgington and N. C. Greenham, *Journal of the American Chemical Society*, 2016, **138**, 2941-2944.
23. J. Zhang, Y. Yang, H. Deng, U. Farooq, X. Yang, J. Khan, J. Tang and H. Song, *ACS Nano*, 2017, **11**, 9294-9302.
24. B. Yang, J. Chen, F. Hong, X. Mao, K. Zheng, S. Yang, Y. Li, T. Pullerits, W. Deng and K. Han, *Angewandte Chemie*, 2017, **129**, 12645-12649.
25. P. Vashishtha, G. V. Nutan, B. E. Griffith, Y. Fang, D. Giovanni, M. Jagadeeswararao, T. C. Sum, N. Mathews, S. G. Mhaisalkar and J. V. Hanna, *Chemistry of Materials*, 2019, **31**, 9003-9011.
26. Y. Li, P. Vashishtha, Z. Zhou, Z. Li, S. B. Shivarudraiah, C. Ma, J. Liu, K. S. Wong, H. Su and J. E. Halpert, *Chemistry of Materials*, 2020.
27. P. Vashishtha, T. J. Hooper, Y. Fang, D. Kathleen, D. Giovanni, M. Klein, T. C. Sum, S. G. Mhaisalkar, N. Mathews and T. White, *Nanoscale*, 2021, **13**, 59-65.
28. B. Yang, X. Mao, F. Hong, W. Meng, Y. Tang, X. Xia, S. Yang, W. Deng and K. Han, *Journal of the American Chemical Society*, 2018, **140**, 17001-17006.
29. Y. Liu, Y. Jing, J. Zhao, Q. Liu and Z. Xia, *Chemistry of Materials*, 2019, **31**, 3333-3339.
30. F. Locardi, M. Cirignano, D. Baranov, Z. Dang, M. Prato, F. Drago, M. Ferretti, V. Pinchetti, M. Fanciulli and S. Brovelli, *Journal of the American Chemical Society*, 2018, **140**, 12989-12995.
31. N. Chen, T. Cai, W. Li, K. Hills-Kimball, H. Yang, M. Que, Y. Nagaoka, Z. Liu, D. Yang and A. Dong, *ACS Applied Materials & Interfaces*, 2019, **11**, 16855-16863.
32. G. Volonakis, M. R. Filip, A. A. Haghighirad, N. Sakai, B. Wenger, H. J. Snaith and F. Giustino, *Journal of Physical Chemistry Letters*, 2016, **7**, 1254-1259.
33. G. Volonakis, A. A. Haghighirad, R. L. Milot, W. H. Sio, M. R. Filip, B. Wenger, M. B. Johnston, L. M. Herz, H. J. Snaith and F. Giustino, *Journal of Physical Chemistry Letters*, 2017, **8**, 772-778.
34. J. Zhou, Z. Xia, M. S. Molokeev, X. Zhang, D. Peng and Q. Liu, *Journal of Materials Chemistry A*, 2017, **5**, 15031-15037.
35. W. Meng, X. Wang, Z. Xiao, J. Wang, D. B. Mitzi and Y. Yan, *Journal of Physical Chemistry Letters*, 2017, **8**, 2999-3007.
36. T. Hu, M. D. Smith, E. R. Dohner, M.-J. Sher, X. Wu, M. T. Trinh, A. Fisher, J. Corbett, X.-Y. Zhu and H. I. Karunadasa, *Journal of Physical Chemistry Letters*, 2016, **7**, 2258-2263.
37. M. Kibbou, Z. Haman, I. Bouziani, N. Khossossi, Y. Benhouria, I. Essaoudi, A. Ainane and R. Ahuja, *Current Applied Physics*, 2020.
38. J. C. Dahl, W. T. Osowiecki, Y. Cai, J. K. Swabeck, Y. Bekenstein, M. Asta, E. M. Chan and A. P. Alivisatos, *Chemistry of Materials*, 2019, **31**, 3134-3143.
39. J. Luo, X. Wang, S. Li, J. Liu, Y. Guo, G. Niu, L. Yao, Y. Fu, L. Gao and Q. Dong, *Nature*, 2018, **563**, 541-545.

40. F. Locardi, E. Sartori, J. Buha, J. Zito, M. Prato, V. Pinchetti, M. L. Zaffalon, M. Ferretti, S. Brovelli and I. Infante, *ACS Energy Letters*, 2019, **4**, 1976-1982.
41. C.-Y. Wang, P. Liang, R.-J. Xie, Y. Yao, P. Liu, Y. Yang, J. Hu, L. Shao, X. W. Sun and F. Kang, *Chemistry of Materials*, 2020.
42. C. Wang, Y. Liu, Y. Guo, L. Ma, Y. Liu, C. Zhou, X. Yu and G. Zhao, *Chemical Engineering Journal*, 2020, **397**, 125367.
43. F. Zhao, Z. Song, J. Zhao and Q. Liu, *Inorganic Chemistry Frontiers*, 2019, **6**, 3621-3628.
44. A. Karmakar, G. M. Bernard, A. Meldrum, A. O. Oliynyk and V. K. Michaelis, *Journal of the American Chemical Society*, 2020, **142**, 10780-10793.
45. C. J. Pickard and R. Needs, *Journal of Physics: Condensed Matter*, 2011, **23**, 053201.
46. S. J. Clark, M. D. Segall, C. J. Pickard, P. J. Hasnip, M. I. Probert, K. Refson and M. C. Payne, *Zeitschrift für Kristallographie-Crystalline Materials*, 2005, **220**, 567-570.
47. C. J. Pickard and F. Mauri, *Physical Review B*, 2001, **63**, 245101.
48. J. R. Yates, C. J. Pickard and F. Mauri, *Physical Review B*, 2007, **76**, 024401.
49. Y. Bekenstein, J. C. Dahl, J. Huang, W. T. Osowiecki, J. K. Swabeck, E. M. Chan, P. Yang and A. P. Alivisatos, *Nano Letters*, 2018, **18**, 3502-3508.
50. L. Zhang, Y. Fang, L. Sui, J. Yan, K. Wang, K. Yuan, W. L. Mao and B. Zou, *ACS Energy Letters*, 2019, **4**, 2975-2982.
51. F. Moser and S. Lyu, *Journal of Luminescence*, 1971, **3**, 447-458.
52. F. Benachenhou, G. Mairesse, G. Nowogrocki and D. Thomas, *Journal of Solid State Chemistry*, 1986, **65**, 13-26.
53. T. Guedira, J. Wignacourt, M. Drache, A. Lorriaux-Rubbens and F. Wallart, *Phase Transitions*, 1988, **13**, 81-85.
54. A. R. Denton and N. W. Ashcroft, *Physical Review A*, 1991, **43**, 3161.
55. B. Luo, Y.-C. Pu, Y. Yang, S. A. Lindley, G. Abdelmageed, H. Ashry, Y. Li, X. Li and J. Z. Zhang, *Journal of Physical Chemistry C*, 2015, **119**, 26672-26682.
56. A. Kanwat, N. Yantara, Y. F. Ng, T. J. Hooper, P. J. S. Rana, B. Febriansyah, P. C. Harikesh, T. Salim, P. Vashishtha and S. G. Mhaisalkar, *ACS Energy Letters*, 2020.
57. B. Zhang, M. Wang, M. Ghini, A. E. Melcherts, J. Zito, L. Goldoni, I. Infante, M. Guizzardi, F. Scotognella and I. Kriegel, *ACS Materials Letters*, 2020, **2**, 1442-1449.
58. T. Chen, M. Zhou, W. Chen, Y. Zhang, S. Oua and Y,Liu, *Sustainable Energy Fuels*, 2021,**5**, 3598-3605.
59. Y. Li, Z. Shi, L. Lei, S. Li, D. Yang, D. Wu, T. Xu, Y. Tian, Y. Lu, Y. Wang, L. Zhang, X. Li, Y. Zhang, G. Du and C. Shan, *Advanced Materials Interfaces* 2019, **6**, 1900188.

TOC

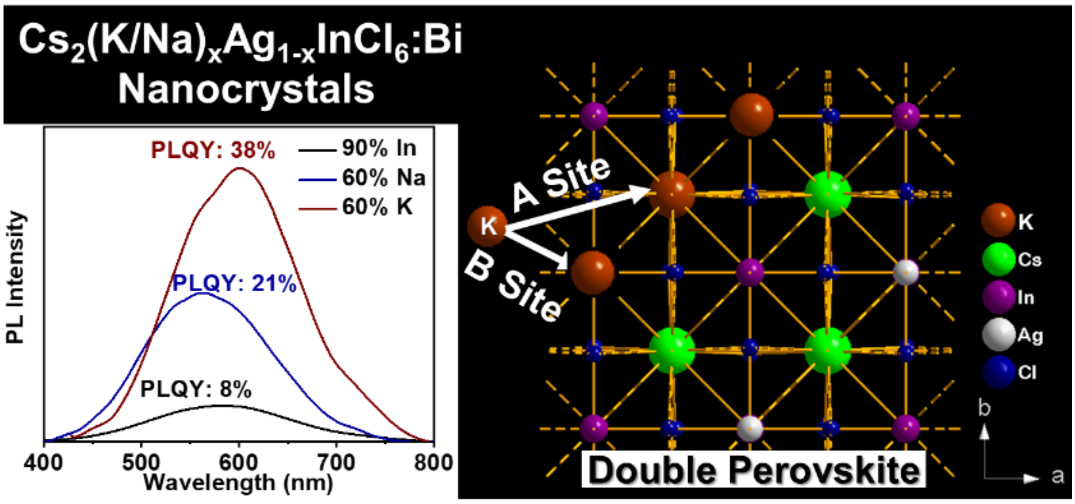

Potassium substituted double perovskite nanocrystals of the form $Cs_2K_xAg_{1-x}InCl_6$:Bi (x = 0 - 1) exhibit improved PLQY behaviour and structural diversity.